Journal for ImmunoTherapy of Cancer

Neoantigen architectures define immunogenicity and drive immune evasion of tumors with heterogenous neoantigen expression

Malte Roerden,[1] Andrea B Castro,[2] Yufei Cui,[1,3] Noora Harake ,[1] Byungji Kim,[1] Jonathan Dye,[1] Laura Maiorino,[1] Forest M White,[1,3] Darrell J Irvine,[1,3,4,5] Kevin Litchfield,[2] Stefani Spranger [1,4,6]

To cite: Roerden M, Castro AB, Cui Y, *et al*. Neoantigen architectures define immunogenicity and drive immune evasion of tumors with heterogenous neoantigen expression. *Journal for ImmunoTherapy of Cancer* 2024;**12**:e010249. doi:10.1136/jitc-2024-010249

► Additional supplemental material is published online only. To view, please visit the journal online (https://doi.org/10.1136/jitc-2024-010249).

SITC Annual Meeting 2023

Received 01 August 2024

Accepted 10 October 2024

Check for updates

© Author(s) (or their employer(s)) 2024. Re-use permitted under CC BY-NC. No commercial re-use. See rights and permissions. Published by BMJ.

For numbered affiliations see end of article.

Correspondence to
Dr Stefani Spranger;
spranger@mit.edu

ABSTRACT

Background Intratumoral heterogeneity (ITH) and subclonal antigen expression blunt antitumor immunity and are associated with poor responses to immune-checkpoint blockade immunotherapy (ICB) in patients with cancer. The underlying mechanisms however thus far remained elusive, preventing the design of novel treatment approaches for patients with high ITH tumors.

Methods We developed a mouse model of lung adenocarcinoma with defined expression of different neoantigens (NeoAg), enabling us to analyze how these impact antitumor T-cell immunity and to study underlying mechanisms. Data from a large cancer patient cohort was used to study whether NeoAg architecture characteristics found to define tumor immunogenicity in our mouse models are linked to ICB responses in patients with cancer.

Results We demonstrate that concurrent expression and clonality define NeoAg architectures which determine the immunogenicity of individual NeoAg and drive immune evasion of tumors with heterogenous NeoAg expression. Mechanistically, we identified concerted interplays between concurrent T-cell responses induced by cross-presenting dendritic cells (cDC1) mirroring the tumor NeoAg architecture during T-cell priming in the lymph node. Depending on the characteristics and clonality of respective NeoAg, this interplay mutually benefited concurrent T-cell responses or led to competition between T-cell responses to different NeoAg. In tumors with heterogenous NeoAg expression, NeoAg architecture-induced suppression of T-cell responses against branches of the tumor drove immune evasion and caused resistance to ICB. Therapeutic RNA-based vaccination targeting immune-suppressed T-cell responses synergized with ICB to enable control of tumors with subclonal NeoAg expression. A pan-cancer clinical data analysis indicated that competition and synergy between T-cell responses define responsiveness to ICB in patients with cancer.

Conclusions NeoAg architectures modulate the immunogenicity of NeoAg and tumors by dictating the interplay between concurrent T-cell responses mediated by cDC1. Impaired induction of T-cell responses supports immune evasion in tumors with heterogenous NeoAg expression but is amenable to NeoAg architecture-informed vaccination, which in combination with ICB portrays a promising treatment approach for patients with tumors exhibiting high ITH.

WHAT IS ALREADY KNOWN ON THIS TOPIC

⇒ Clonal neoantigens (NeoAg) have been identified as key targets eliciting antitumor immune responses and the clonality of NeoAg is a key determinant for the responsiveness to immune-checkpoint blockade therapy across many solid tumor entities. It has been demonstrated experimentally that intratumoral heterogeneity (ITH) and subclonal NeoAg expression blunt the induction of antitumor T-cell responses. Yet, how this is mediated mechanistically remained unknown.

WHAT THIS STUDY ADDS

⇒ We show that the reduced immunogenicity of tumors with heterogenous NeoAg expression is based on an impaired induction of antitumor T-cell responses due to a reduction of synergistic effects between concurrent T-cell responses as well as a suppression of T-cell responses to tumor branches in immunodominance hierarchies. Synergy and competition between concurrent T-cell responses are mediated by cross-presenting dendritic cells mirroring the tumor NeoAg architecture during T-cell priming in the tumor-draining lymph node. While this concerted interplay can be beneficial in clonal tumors, it can drive immune evasion in tumors with heterogenous NeoAg expression. We further demonstrate that therapeutic vaccination can overcome the reduced immunogenicity of these tumors when tailored to their respective NeoAg architecture.

HOW THIS STUDY MIGHT AFFECT RESEARCH, PRACTICE OR POLICY

⇒ The study provides novel mechanistic insights into the strong clinical association of tumor and NeoAg clonality with immunogenicity. This improved understanding will fuel further research to develop treatment approaches for tumors with high ITH and strongly suggests that the design of cancer vaccines should be informed by the tumor NeoAg architecture.

BACKGROUND

Cytotoxic CD8$^+$ T cells can specifically recognize and eliminate cancer cells when detecting tumor-derived antigens presented via major histocompatibility complex (MHC) molecules.[1] Mutated neoantigens (NeoAg) are tumor-specific antigens derived from cancer cell-specific genetic alterations and can be effective targets for T cell-mediated tumor cell killing.[2–4] The quality or immunogenicity of individual NeoAg is defined by multiple parameters, most importantly MHC-binding characteristics, and the likelihood of recognition by T cells.[5 6] Recent findings however indicate that NeoAg architectures portray an additional key determinant for the immunogenicity of NeoAg, thus impacting the strength of the antitumor T-cell response.[7–9] NeoAg architectures are defined by the overall abundance as well as the clonality of specific NeoAg[9] and are shaped during tumor evolution, which frequently leads to a coexistence of phenotypically distinct tumor subclones.[10–12] This intratumoral heterogeneity (ITH) is inherent to most solid cancers[10–12] and can lead to the expression of clonal as well as subclonal NeoAg, which are respectively shared between all, or limited to a fraction of tumor cells. ITH and subclonal NeoAg expression have been shown to effectively blunt antitumor T-cell responses.[13 14] Moreover, clinical data have established NeoAg clonality as a key predictor of response to immune-checkpoint blockade immunotherapy (ICB) in patients with cancer.[14–16] While this clinical correlation is well established,[16] it is poorly understood how ITH impairs antitumor immunity on a mechanistic level.

NeoAg architectures could impact antitumor T-cell responses both through the abundance as well as the clonality of tumor NeoAg. Concurrent T-cell responses targeting distinct antigens are known to influence one another,[7 8] but the determinants dictating their interplay during tumor evolution are incompletely understood. The establishment of antigen hierarchies between CD8$^+$ T-cell responses has been described in murine cancer models,[7] mirroring the interplay between T-cell responses observed in viral disease.[17] In these hierarchies, a dominant NeoAg-specific immune response is enhanced at the expense of subdominant immune responses.[7] Enhanced NeoAg-specific responses on the other hand can be observed in the context of CD4$^+$ T-cell response-mediated help based on tumor expression of MHC-II-restricted NeoAg[18–21] and, as described more recently, in the context of concurrent CD8$^+$ T-cell responses to MHC-I-restricted NeoAg lacking observable immunodominance.[8] How NeoAg clonality and the interplay between T-cell responses act together to impact antitumor immunity in complex, subclonal NeoAg architectures is unknown. This is a critical issue, as human cancers, with few exceptions, are subclonal diseases, typically consisting of one to three distinct tumor subclones.[10] Patients with tumors exhibiting high ITH currently derive little or no benefit from ICB.[9 16] A better understanding of how ITH blunts antitumor immune responses could enable the development of novel treatment approaches for patients. A deepened understanding is further pivotal for the design of multivalent cancer vaccines. Defining ideal targets and antigen combinations could allow therapeutically leveraging of (neo-)antigen architectures to maximize antitumor immunity.

In this study, we therefore investigated how NeoAg architectures impact antitumor T-cell responses. We used a reductionist preclinical mouse model with defined NeoAg expression to decipher the interplay between concurrent NeoAg-specific CD8$^+$ T-cell responses. This further allowed the modeling of complex, clinically relevant NeoAg architectures to study the impact of this interplay in tumors with heterogenous NeoAg expression. We found that antigen presentation by cross-presenting dendritic cells (cDC1) in the lymph node mirrors tumor NeoAg architectures as they orchestrate the interplay between concurrent T-cell responses. Mediated by cDC1, NeoAg expression patterns in the tumor thus define the NeoAg architecture-dependent immunogenicity (NADi) of individual NeoAg and tumor subclones. In tumors with heterogenous NeoAg expression, suppressed NADi drove immune evasion and mediated resistance to ICB. Therapeutic RNA-based vaccination targeting suppressed NeoAg responses synergized with ICB to overcome impaired immunogenicity of tumors with heterogenous NeoAg expression and enabled tumor control. Combining ICB with clonal NeoAg-targeting vaccination might thus represent a tailored treatment approach for patients with tumors exhibiting high ITH.

MATERIALS AND METHODS

Mice

C57BL/6 wildtype mice (B6, strain #000664) and B6-CD45.1$^+$ mice (strain #002014) were purchased from Jackson Laboratories. Rag2-knockout mice (Rag2$^{-/-}$, strain #008449) were purchased from Jackson Laboratories and bred in-house. Mice were housed under specific pathogen-free conditions at the Koch Institute animal facility. Mice were gender-matched and age-matched for experiments (6–12 weeks old at the time of experimentation). All animal procedures were approved by the Committee on Animal Care at MIT.

Tumor cell lines, cell culture and tumor injections

Parental cancer cell lines KP1233 and RMA-S were gifts from Tyler Jacks (Koch Institute for Integrative Cancer Research at MIT). KP6S was subcloned from KP1233. Tumor cell lines were cultured at 37°C and 5% CO_2 in complete media (Dulbecco's Modified Eagle Medium (DMEM) (Gibco) supplemented with 10% heat-inactivated Fetal Bovine Serum (FBS) (Atlanta Biologicals), 1% penicillin/streptomycin (Gibco), and 20 mM 4-(2-Hydroxyethyl)piperazine-1-ethanesulfonic acid (HEPES) (Gibco)). For tumor injections, tumor cells were harvested by trypsinization (Gibco), washed three times with phosphate-buffered saline (PBS) (Gibco), resuspended in PBS and 1×10^6 tumor cells were injected subcutaneously on the flank. For tumor

outgrowth experiments, the subcutaneous tumor area (length×width) was measured every 2–3 days using digital calipers.

Generation of NeoAg expression vectors and NeoAg-expressing cell lines

To generate NeoAg expression vectors, a fluorescent protein (mCherry, ZsGreen or Cerulean) was first cloned into the backbone vectors pLV-EF1α-IRES-puro and pLV-EF1α-IRES-Blast (Addgene plasmids #85132 and #85133). These were then linearized by enzymatic digestion with HF-SpeI and HF-EcoRI restriction enzymes (NEB) before oligonucleotides (Genewiz) containing the NeoAg-genetic barcode sequences were cloned into the linearized vectors. Fluorophores were expressed upstream of the NeoAg, separated by a spacer sequence. NeoAg sequences encoded for the mutant peptide flanked by two amino acid overhangs of the wildtype sequence on each side. When expressing multiple NeoAg, these were separated by spacer sequences. The length of the NeoAg-encoding sequence within the construct was kept constant between different constructs (online supplemental figure S1A). The resulting constructs were amplified and sequenced for accuracy. Constructs were subsequently used to generate third generation lentiviruses using Lenti-X 293 T cells. A functional lentivirus titer was obtained through serial dilution of the virus and infection of KP6S cells followed by selection with puromycin (Gibco) or blasticidin (Gibco) (7 and 10 days, respectively). Cells were then fixed (10% formalin) and stained with crystal violet stain before colonies were counted to determine the functional virus titer. To generate NeoAg-expressing cell lines, the parental line KP6S was transduced with titered lentiviruses at an multiplicity of infection (MOI) of 0.1, diluted in complete media supplemented with 4 µg/mL protamine sulfate (Sigma-Aldrich). The virus-containing media was replaced with complete media after 24 hours, selection was started 48 hours after transduction using selection media (containing either 2 µg/mL puromycin or 10 µg/mL blasticidin). Flow cytometry-based analysis of fluorescent protein expression was used to confirm transduction and to determine construct expression levels (online supplemental figure S1B).

Neoantigens and peptides

Naturally presented, endogenous NeoAg were identified in the literature.[4 13 20 22 23] NeoAg sequences and sources are listed in online supplemental table S1. MHC-binding prediction was performed using NetMHCpan-4.1.[24] NeoAg peptides were purchased from GenScript (Adpgk, Spb2, Aatf, Cpne1, Lama4, Alg8) and Peptide2 (Intb1) at >95% purity and reconstituted in 100% Dimethylsulfoxide (DMSO) at a stock concentration of 10 µg/µL.

Tissue processing for flow cytometry, cell sorting and ELISpot

Tumors, tumor-draining lymph node (tdLN) and spleens were resected and stored in Roswell Park Memorial Institute Medium (RPMI) (Gibco) or tumor digestion buffer (RPMI supplemented with 250 µg/mL Liberase (Roche) and 2 mg/mL DNAse (Roche)) on ice before further processing. LN were either directly mashed through a 70 mm filter into RPMI (Gibco) for T-cell analysis, or processed using a method adapted from Ruhland *et al*[25] as described previously.[26] Spleens were mashed through 70 µm filters to obtain a single-cell solution and red blood cells were lysed with ACK lysis buffer (Gibco) for 5 min on ice. Splenocytes were washed twice with RPMI before further processing. Tumors were weighed and minced using razor blades before enzymatic digestion at 37°C for 30 min. Digested tumors were mashed through 70 µm filters to obtain a single-cell solution. For ≥day 10 tumor analyses, lymphocytes were isolated using Ficoll (Sigma-Aldrich). Cells were washed twice with RPMI before further processing.

Flow cytometry staining and analysis

For flow cytometry staining, cells were first resuspended in Fluorescence-activated cell sorting (FACS) buffer (PBS (Gibco) with 1% FBS (Atlanta Biologicals) and 2 mM EDTA (Invitrogen)) containing Fixable Viability Dye eFluor 780 to distinguish live and dead cells and αCD16/CD32 (clone 93, BioLegend) to prevent non-specific antibody binding, and incubated for 20 min at 4°C. Cells were then washed with FACS buffer and stained for surface proteins using fluorophore-conjugated antibodies resuspended in FACS buffer. Following surface staining, cells were washed twice with FACS buffer and analyzed directly or fixed for downstream intracellular staining and/or analysis the next day. Cell fixation was performed using the Foxp3 Transcription Factor Fixation/Permeabilization Buffer (eBioscience) following manufacturer's instructions. Following fixation, cells were washed twice with FACS buffer and stained for intracellular markers overnight at 4°C. Finally, cells were washed twice with FACS buffer prior to flow cytometry analysis. Precision count beads (BioLegend) were used to determine the total numbers of cells present in a sample. Sample acquisition was performed on BD flow cytometers (FACSCanto II, Symphony A3, Fortessa) and analyzed using FlowJo V.10 (TreeStar). For cell sorting, the surface staining was performed as described above under sterile conditions and cells were sorted on an FACSAria III sorter (BD). For $CD8^+$ T-cell analyses, cells were pre-gated on live, singlets, $CD45^+$ (or $CD45.1^+$ when congenically labeled), $CD3e^+$, $CD4^-$, $CD8^+$ surface markers. For DC analyses, cells were pre-gated on live, singlets, $CD45^+$, $CD19^-$, $CD3e^-$, $NK1.1^-$, $Ly6C^+$, $MHC\text{-}II^+$, $F4/80^-$, $CD11c^+$ and $mCherry^+$/$ZsGreen^+$ when applicable.

Tetramers and tetramer-staining

Biotinylated MHC monomers were generated at the NIH Tetramer Core Facility and tetramerized using fluorophore-linked streptavidin (premium-grade PE-Streptavidin or APC-Streptavidin (Invitrogen)). Cells were pre-incubated with 50 nM Dasatinib (Sigma-Aldrich) for 25 min at 37°C to enhance tetramer binding[27] before

Table 1 Adoptively transferred CD8+ T cells

Recipient mice	Single NeoAg tumor-bearing donors #1	Single NeoAg tumor-bearing donors #2	Multi NeoAg tumor-bearing donors	Naïve mice
Naïve	–	–	–	10×10^6 cells
Single NeoAg	5×10^6 cells	5×10^6 cells	–	–
NeoAg competition/ synergy	–	–	5×10^6 cells	5×10^6 cells

NeoAg, neoantigens.

staining at 4°C for 30 min together with surface marker staining.

Adoptive bulk CD8+ and tetramer-sorted T-cell transfers

Splenocytes were isolated from spleens of naïve or tumor-bearing mice on day 7 after tumor injection and CD8+ T cells were enriched using magnetic cell separation (CD8a+T Cell Isolation Kit (Miltenyi Biotec)). For bulk CD8+ T-cell transfers, 5×10^6 CD8+ T cell-enriched cells per donor group were transferred into tumor-bearing recipient mice (bearing single NeoAg-expressing tumors on opposite flanks; day 4 after tumor injection). The total number of transferred CD8+ T cell-enriched cells was kept constant between recipient groups (table 1).

For the transfer of Tetramer-sorted cells, CD8+ T cell-enriched cells were stained, and tetramer-positive cells were sorted on an FACSAria III cell sorter (BD). 5,000 tetramer-positive cells per mouse were then transferred into tumor-bearing (day 4 after tumor injection) recipient mice.

Interferon-γ ELISpot assay

Enzyme-linked immunosorbent spot (ELISpot) plates (EMD Millipore) were coated overnight at 4°C with anti-interferon (IFN)-γ capture antibody (BD Biosciences). Plates were washed and blocked with complete media for 2 hours at room temperature. Splenocytes were plated in complete media at 0.5×10^6 or 1×10^6 cells/well with either 50 ng/µL (10 µg/well) NeoAg peptide, negative control (complete media) or positive control (complete media supplemented with 100 ng/mL PMA (Sigma-Aldrich) and 1 mg/mL ionomycin (Sigma-Aldrich)). Plates were incubated overnight (16–18 hours) at 37°C and 5% CO_2 and developed using a mouse IFN-γ ELISpot kit (BD Biosciences), following manufacturer's instructions. After drying (overnight at room temperature), spot counts were determined using an ImmunoSpot (CTL) ELISpot reader.

In vivo cytotoxicity assay

In vivo cytotoxicity was determined as described previously.[20] In brief, donor splenocytes were isolated from naïve B6 and B6-CD45.1+ mice and stained with either carboxyfluorescein succinimidyl ester (CFSE) (0.5 µM or 5 µM for $CFSE^{low}$ and $CFSE^{hi}$) or cell trace violet (CTV) (0.5 µM or 5 µM for CTV^{low} and CTV^{hi}). Cells were washed with PBS and pulsed with 10 µg/mL peptide for 2 hours in lymphocyte media (complete media supplemented with non-essential amino acids (Thermo Fisher), 1 mM sodium pyruvate (Thermo Fisher) and 55 µM ß-mercaptoethanol (Gibco). Unpulsed splenocytes served as a control population. Cells were washed three times with PBS, mixed in 50/50 ratios and 5×10^6 cells were retro-orbitally transferred into day 10 tumor-bearing recipient mice. After 20 hours, spleens were harvested and the ratio of peptide-pulsed to unpulsed cells was determined by flow cytometry. The ratio was normalized to the ratio determined in naïve control mice. Per cent specific lysis was calculated as (1 − (naïve control ratio/experimental ratio)) × 100.

Peptide:MHC binding assays

Affinity of peptide:MHC (pMHC) binding was determined using TAP-deficient RMA-S cells. In brief, RMA-S cells were first incubated at 26°C for 16 hours to increase the surface expression of empty MHC molecules.[28] Cells were then incubated with peptide at 26°C for 2 hours before degrading empty MHC molecules at 37°C for 1 hour. The relative quantity of peptide-stabilized MHC molecules was assessed by staining with anti-H2-Db and/or anti-H2-Kb antibodies for 20 min at 4°C followed by fixation and flow cytometry-based analysis.

DNA extraction and quantitative PCR

Genomic DNA was isolated using the GenElute Mammalian Genomic DNA Miniprep Kit (Sigma-Aldrich) following manufacturer's instructions. Isolated DNA was quantified by NanoDrop and diluted to 1 ng/µL for quantitative PCR (qPCR). Standard curves were generated using genomic DNA extracted from respective tumor cell lines. qPCR was performed using an SYBR Green PCR Master Mix (Applied Biosystems) and run on a StepOne Real-Time PCR System (Applied Biosystems). Genetic barcode copy numbers were interpolated using a standard curve for each barcode. Subclonal fractions were normalized using an aliquot of the injected tumor cell solution as a reference.

In vivo antibody treatments

CD8+ T-cell depletion: CD8+ T cells were depleted in vivo by administering 200 µg anti-CD8-antibody (Bio X Cell) intraperitoneally (i.p.) 2 days prior to tumor injection followed by 100 µg twice weekly during ongoing experiments. H2 allele-specific blockade: Allele-specific H2-Kb

in vivo blockade was performed by administering 400 µg anti-H2-Kb-antibody (Bio X Cell) i.p. 1 day prior to tumor injection followed by 200 µg on day 2 and 4 after tumor injection. Immune checkpoint blockade therapy (ICB): Mice were injected i.p. with 100 µg of anti-cytotoxic T-lymphocyte associated protein 4 (Bio X Cell) and 100 µg anti-programmed death-ligand 1 PD-L1 (Bio X Cell) in PBS on days 7, 10, 13 and 16 after tumor injection.

Replicon RNA synthesis

Venezuelan equine encephalitis virus (VEE) replicon plasmid DNA was prepared based on mutant constructs and cloned after the subgenomic promoter as described previously.[29–31] VEE DNA was linearized via endonuclease digestion and purified with PureLink PCR Purification columns (Thermo Fisher) following manufacturer's instructions. To synthesize RNA, 20 µL in vitro transcription (IVT) reactions were performed using the HiScribe T7 High Yield RNA Synthesis Kit (NEB) and 1–2 µg of linear DNA template (scaled as needed). The IVT product was purified using PureLink RNA Mini columns (Thermo Fisher) following manufacturer's instructions. RNA was then capped and methylated using the ScriptCap Cap 1 Capping System (CellScript) following manufacturer's instructions, after which RNA was purified a final time using PureLink RNA Mini columns. The quality of the resulting replicons was assessed using UV-Vis spectrophotometry and gel electrophoresis.

Lipid nanoparticle formulation and replicon RNA vaccines

Self-replicating (replicon) RNA vaccines were designed and synthesized as described previously.[32] Lipid nanoparticles (LNPs) were composed of N1,N3,N5-tris(3-(didodecylamino)propyl)benzene-1,3,5-tricarboxamide (TT3), (6Z,9Z,28Z,31Z)-Heptatriaconta-6,9,28,31-tetraen-19-yl 4-(dimethylamino) butanoate (DLin-MC3-DMA; MedChemExpress), 1,2-dioleoyl-sn-glycero-3-phosphoethanolamine (DOPE; Avanti Polar Lipids), Cholesterol (Avanti Polar Lipids), and 1,2-dimyristoyl-rac-glycero-3-methoxypolyethylene glycol-2000 (DMG-PEG2k; Avanti Polar Lipids), mixed at a molar ratio of 10:25:20:40:5 in ethanol. Replicon-RNA was diluted in 10 mM citrate buffer (pH 3.0) and formulated in LNPs at amine-to-phosphate (N/P) ratio of 2:1 through microfluidic nanoprecipitation (NanoAssemblr Ignite instrument, Precision NanoSystems) at a volume ratio of 1:2 (organic:aqueous) and flow rate of 12 mL/min. Replicon-RNA containing LNPs were dialyzed against PBS prior to intramuscular injection into the gastrocnemius muscle (1 µg RNA/dose).

Bone marrow-derived dendritic cell generation and culture

Bone marrow-derived dendritic cells (BMDCs) were generated as described previously.[33] In brief, bone marrow was isolated from femurs and tibias of naïve mice, red blood cells were lysed using ACK lysis buffer, and remaining cells were washed and cultured in BMDC media (RPMI supplemented with 10% FBS, 1 mM HEPES, 55 µM β-mercaptoethanol, non-essential amino acids, 2 ng/mL murine GM-CSF (BioLegend), and 100 ng/mL human Flt-3L-Ig (Bio X Cell). Media was changed every 2 days and cells were split on day 4 before harvest on day 7. BMDCs were frozen in 10% DMSO (Sigma-Aldrich) in FBS (Atlanta Biologicals) and stored in liquid nitrogen. BMDCs were phenotyped using flow cytometry.

ß2-mikroglobulin (B2M)-knockout cell line generation

B2M$^{-/-}$ cell lines were generated as described previously.[33] In brief, the KP6S parental line was transiently transfected with three pooled CRISPR guides targeting exon 2 of murine B2M cloned into the px459-Cas9-puro vector (Addgene #62988) followed by selection with 2.5 µg/mL puromycin for 48 hours. B2M-KO was confirmed by flow cytometry-based analysis of surface H-2Db/Kb expression. NeoAg-expression in B2M$^{-/-}$ cell lines was engineered as described above.

Tumor cell irradiation and co-culture with BMDCs

To generate tumor debris, tumor cells were trypsinized, counted and irradiated with 20 Gy (gray) on ice before being cultured for 96 hours. Non-adherent tumor debris was then harvested, counted and added to BMDCs (thawed 24 hours earlier). BMDCs were co-cultured with tumor cell debris for 18 hours, collected, washed with PBS and flash-frozen in liquid nitrogen before processing for mass spectrometry.

Heavy isotope-labeled peptide synthesis

Heavy amino acid labeled Alg8-peptides were generated at the Biopolymers and Proteomics core facility at MIT. Synthesized peptides were cleaved using a standard cleavage cocktail and purified to >95% using high-performance liquid chromatography (HPLC). Molecular weight was confirmed using a MALDI mass spectrometer (Bruker microflex). Heavy isotope-labeled amino acids used for synthesis were purchased from Cambridge Isotope Laboratories (table 2).

Generation of recombinant heavy isotope-labeled peptide MHCs

Heavy amino acid-labeled Alg8 peptides and positive control peptides (provided by manufacturer) were loaded on recombinant, empty mouse H2-Kb monomers (easYmers, Immunaware) according to manufacturer's

Table 2

HIP reference peptide	Sequence	Amount added in IP
1H	IT(+5)YTWTRL	0.1 fmol
2H	IT(+5)YT(+5)WTRL	1 fmol
3H	IT(+5)YT(+5)WT(+5)RL	10 fmol
4H	I(+7)T(+5)YT(+5)WT(+5)RL	100 fmol

HIP, heavy isotope-labeled peptide; IP, immunoprecipitation .

protocol. The concentration of stable complexes post loading was quantified using a protocol adapted from Flex-T HLA class I ELISA assay (BioLegend).

pMHC isolation

Cell pellets containing 2.2–5×10^6 co-cultured BMDCs were resuspended in 1 mL MHC lysis buffer (20 mM Tris-HCl pH 8.0, 150 mM NaCl, 0.2 mM PMSF (Sigma), 1% CHAPS (Sigma), and 1× Halt Protease/Phosphatase Inhibitor Cocktail (Thermo Scientific)), followed by brief sonication at 4°C (3×10 s microtip sonicator pulses at 30% amplitude) to disrupt cell membranes. Lysates were cleared by centrifugation at 16,000 ×G for 15 min at 4°C. pMHCs were isolated from lysates by immunoprecipitation (IP) and size exclusion filtration, as previously described.[34] In brief, for each sample 0.1 mg of anti-mouse H2-Kb antibody (clone Y-3 clone, InVivoMAb, catalog #BE0172) was conjugated to 20 µL FastFlow Protein A Sepharose bead slurry (Cytiva). Beads were washed 1× with IP wash buffer (20 mM Tris-HCl pH 8.0, 150 mM NaCl), followed by the addition of lysate and known amounts of isotopologue heavy isotope-labeled peptide MHCs (see Table 2 below), and incubated rotating overnight at 4°C to immobilize pMHCs on beads. Beads were washed with 1× TBS and 2× water, and pMHCs were eluted using 10% acetic acid for 20 min at RT. Peptides were isolated from antibody and MHC molecules using a 10 K molecule weight cut-off filter (PALL Life Science), lyophilized, and stored at −80°C until analysis.

Mass spectrometry data acquisition

Samples were analyzed using an Orbitrap Exploris 480 mass spectrometer (Thermo Scientific) coupled with an UltiMate 3000 RSLC Nano LC system (Dionex), Nanospray Flex ion source (Thermo Scientific), and column oven heater (Sonation). pMHC samples were resuspended in 5 µL of 3% acetonitrile, 0.1% formic acid, and loaded onto a 10–12 cm analytical capillary chromatography column with an integrated electrospray tip (~1 µm orifice), prepared and packed in house (50 µm ID and 1.9 µM C18 beads, ReproSil-Pur) through WPS-3000 autosampler (Dionex).

Survey analyses: Peptides were eluted using a gradient with 6–25% buffer B (70% acetonitrile, 0.1% formic acid) for 53 min, 25–45% for 12 min, 45–97% for 3 min, and 97–3% for 1 min. Standard mass spectrometry parameters were as follows: spray voltage, 2.5 kV; no sheath or auxiliary gas flow; heated capillary temperature, 280°C. The Exploris was operated in data-dependent acquisition (DDA) mode with an inclusion list of the 4H trigger peptide. Full scan mass spectra (300–1,500 m/z, 60,000 resolution) were detected in the orbitrap analyzer after accumulation of 3×10^6 ions (normalized AGC target of 300%) or 50 ms. For every full scan, up to 20 ions were subsequently isolated if the m/z was within ±5 ppm of the targeted 4H trigger peptide and reached a minimum intensity threshold of 1×10^5. Ions were collected with a maximum injection time of 250 ms, normalized AGC target=1000%, and fragmented by higher energy collisional dissociation (HCD) with a collision energy (CE): 30%. A library of acquired spectra was generated using Skyline software for SureQuant-IsoMHC targeted analyses.

SureQuant-IsoMHC targeted analyses: The custom SureQuant acquisition template available in Thermo Orbitrap Exploris Series 2.0 was used for this method. All acquisition parameters for heavy labeled Alg8 isotopologues are located within a distinct 4-node branch stemming from a full scan node. In the full scan, the trigger 4H peptide m/z and intensity thresholds are defined in the "Targeted Mass" filter node as 1% of the intensity from the DDA survey run. Next, parameters for the low resolution, trigger peptide MS2 scan are defined, followed by the "Targeted Mass Trigger" filter node, which defines the six product ions used for pseudo-spectral matching. To connect each set of product ions within the targeted mass trigger node to a given precursor mass, a group ID feature was used to define the precursor m/z associated with each group of product ions. Finally, the isolation offset (m/z) corresponding to each of the four MS2 scans of the endogenous and 1–3 hours peptides was defined in the scan parameters within each node. Standard mass spectrometry (MS) parameters for SureQuant acquisition were as follows: spray voltage: 2.5 kV, no sheath or auxiliary gas flow, heated capillary temperature: 280°C. Full-scan mass spectra were collected with a scan range: 380–1,200 m/z, AGC target value: 300% (3e6), maximum IT: 50 ms, resolution: 120,000. 4H Alg8 peptide matching the m/z (within 10 ppm) and exceeding the intensity threshold defined on the inclusion list were isolated (isolation window 1 m/z) and fragmented (nCE (normalized collision energy): 30%) by HCD with a scan range: 150–1,200 m/z, maximum injection time: automatically determined from the resolution, AGC (Automatic gain control) target value: 1,000% (1e6), resolution: 15,000. A product ion trigger filter next performs pseudo-spectral matching, only triggering an MS2 event of the endogenous target peptide and heavy standard peptides at the defined mass offset if n≥3 product ions are detected from the defined list. If triggered, the subsequent light, 1H, 2H, and 3H peptides MS2 scans are initiated at the defined mass offsets. Scan parameters have the same CE, scan range, and AGC target as the heavy trigger peptide, but with a higher maximum injection time and resolution (3H&2H: max IT: 250 ms, resolution, 120,000; 1H&light: max IT: 1 s, resolution 480,000). Triggered MS2 scans are performed in the following order: 3H, 2H, 1H, light. Ions for pseudo-spectral matching ar listed in table 3.

SureQuant-IsoMHC data analysis

Skyline software was used to quantify the abundance of the standard and endogenous peptide. For each sample, the abundance of each Alg8 peptide (1H, 2H, 3H and light) was approximated using an average of the maximum intensity of the top three product ions across the elution chromatogram. The average intensity of the three heavy Alg8 standards was regressed against the

Table 3

Compound	m/z	Group ID
y7	955.5201	538.3143
y6	849.4619	538.3143
y5	686.3986	538.3143
y4	580.3405	538.3143
y3	394.2611	538.3143
b4	496.2881	538.3143

amount added in IP to generate a standard curve. The absolute amount of endogenous light Alg8 peptide was calculated using the embedded standard curve in each sample. Copies of Alg8 peptide per cell were calculated using the absolute amount and input cell number in the IP.

Human data analysis

Patient with pan-cancer cohort data sets: Data from a total of 922 patients undergoing ICB treatment for the following cancer entities from publicly available studies were gathered and processed in a harmonized manner: Lung cancer,[35–37] colorectal cancer,[38] melanoma,[39–44] gastric cancer,[45] urothelial cancer,[46] renal cancer,[47 48] multiple tumor entities.[49 50]

Preprocessing: Patient FASTQ files were obtained from respective publications. The Sarek V.3.1.1 pipeline[51 52] was used for harmonized alignment and variant calling to hg38. pVACseq via pVACtools V.3.1.3 and vatools V.5.0.1 was used to perform in silico binding affinity predictions of patient NeoAg. HLA-HD V.1.6.1 was used to call patient HLA types. Pyclone V.0.13.1 was used to perform mutation clonality clustering.

Analysis: NeoAg from pVACseq were classified as strong or weak binders according to a NetMHCpan-4.1 percentile rank of <0.5 and <2, respectively. Mutations and their associated NeoAg were classified as clonal if they were found in the pyclone cluster with the greatest number of mutations for each patient. Immunodominance was measured using the greatest number of NeoAg that were strongly presented by any of a patient's HLA alleles.

Statistical analysis

Statistical analyses were performed using GraphPad Prism V.10. Data are shown as mean±SEM, unless otherwise indicated. Comparisons between groups were performed using parametric (Student's t-test, analysis of variance (ANOVA)) or non-parametric tests (Mann-Whitney U test, Kruskal-Wallis test) after testing for normality of data distribution (Shapiro-Wilk test). Tumor outgrowth curves were compared using two-way ANOVA. Correction for multiple comparisons was performed where applicable. P values<0.05 were considered statistically significant (*p<0.05; **p<0.01; ***p<0.001; ****p<0.0001; ns=not significant).

RESULTS

Peptide:MHC binding characteristics alone fail to predict immunogenicity of co-expressed NeoAg

To study the impact of NeoAg architectures on antitumor immune responses, we developed a preclinical mouse model with defined NeoAg architectures. First, to reduce intra-cell line heterogeneity, a subclone of the $Kras^{G12D}$ $Trp53^{-/-}$ (KP) lung adenocarcinoma cell line[53] was generated (KP6S; parental cell line). This cell line was subsequently engineered to express either single or multiple NeoAg linked to a fluorescent protein followed by a genetic barcode (figure 1A, online supplemental figure S1A). Individual or mixes of NeoAg-expressing KP6S derivative cell lines were used to model tumors with clonal and subclonal NeoAg expression, respectively (figure 1A). All engineered NeoAg were previously described, endogenous, naturally MHC-presented NeoAg[13 20 22 23] (figure 1B) and expressed at similar levels (online supplemental figure S1B). Predicted[24] and observed pMHC binding affinities correlated with in vivo immunogenicity of individually expressed NeoAg, as assessed by IFN-γ ELISpot assays and tumor outgrowth experiments (figure 1B–D, (online supplemental figure S1C,D). We categorized NeoAg as strong (highly immunogenic, NeoAg $S_{1\text{-}4}$) and weak (poorly immunogenic, NeoAg $W_{1\text{-}2}$), when their expression respectively did or did not improve tumor control compared with the parental cell line (figure 1C,D, online supplemental figure S1E). $CD8^+$ T-cell depletion resulted in a loss of NeoAg expression-induced tumor control (online supplemental figure S1E), indicating that tumor control was predominantly mediated by NeoAg-specific $CD8^+$ T cells.

Previous work by our group using a reductionist model to compare the clonal or subclonal expression of two NeoAg ($S_{1\ (Adpgk)}$ and $W_{1\ (Aatf)}$) demonstrated that clonal NeoAg expression resulted in enhanced antitumor T-cell immunity.[8] To decipher the dynamic interplay between concurrent T-cell responses and its mechanistic underpinnings systematically, we first used this reductionist system and co-expressed pairs of NeoAg either clonally or subclonally (figure 1E–K). These paired NeoAg models uncovered two consistent patterns of interplay between concurrent NeoAg-specific $CD8^+$ T-cell responses, indicating that the antigenic context contributes to define NeoAg immunogenicity. First, a mutually beneficial interplay was observed between responses against co-expressed weak and strong NeoAg and depended on clonal expression (NeoAg synergy, figure 1E–H). And second, an establishment of immunodominance hierarchies with dominant and subdominant responses was observed between co-expressed strong NeoAg. This observation depended on clonal NeoAg expression as well as restriction to the same MHC allele (NeoAg competition, figure 1I-K).

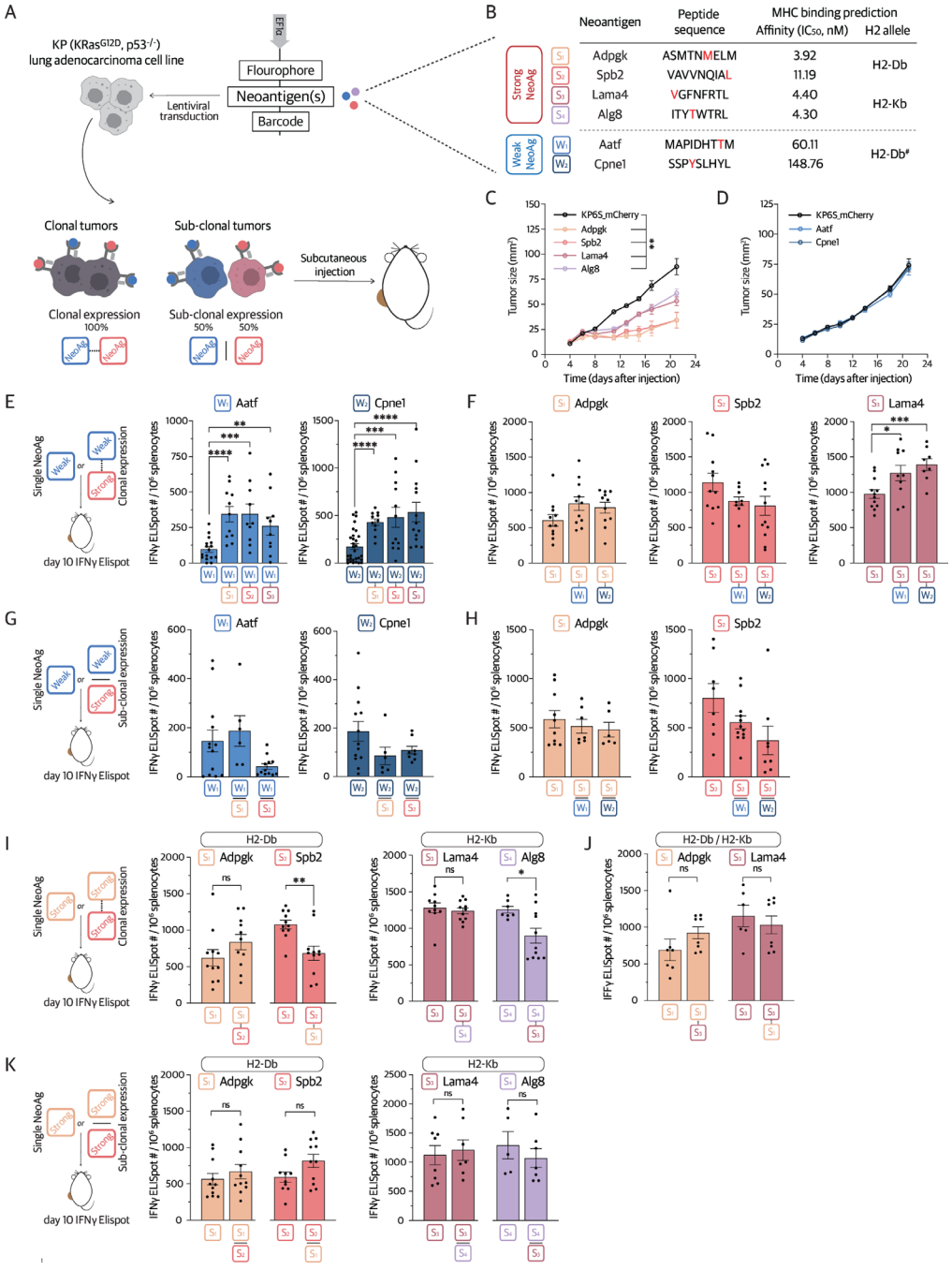

Figure 1 pMHC binding characteristics alone fail to predict immunogenicity of co-expressed NeoAg. (A) Transplantable KP lung adenocarcinoma mouse model, genetically engineered to express single or multiple NeoAg and injected subcutaneously as tumors with clonal or subclonal NeoAg expression. (B) Highly and poorly immunogenic (strong and weak) NeoAg, peptide sequences and pMHC binding predictions using NetMHCpan-4.1. #Cpne1 is predicted to also bind H2-Kb at a lower affinity (IC_{50}=170.9 nM) (C–D) Tumor outgrowth of (C) strong and (D) weak NeoAg-expressing tumors compared with parental cell line tumors. (E–F) IFN-γ ELISpot counts on day 10 after tumor injection for (E) weak and (F) strong NeoAg expressed alone or clonally co-expressed with a (E) strong or (F) weak NeoAg. (G–H) IFN-γ ELISpot counts on day 10 after tumor injection for (G) weak and (H) strong NeoAg expressed alone or subclonally co-expressed with a (G) strong or (H) weak NeoAg. (I–J) IFN-γ ELISpot counts on day 10 after tumor injection for strong NeoAg expressed alone or clonally co-expressed with a second strong NeoAg restricted to (I) the same or (J) a different MHC allele. (Data for single NeoAg $S_{1\ (Adpgk)}$ tumors in (I) and (J) partially from overlapping experiments.) (K) IFN-γ ELISpot counts on day 10 after tumor injection for strong NeoAg expressed alone, or subclonally co-expressed with a second strong NeoAg restricted to the same MHC allele. (Data for single NeoAg $S_{1\ (Adpgk)}$ and $S_{2\ (Spb2)}$ tumors partially from overlapping experiments with (H)). (C–D) Representative display of ≥2 independent experiments (n≥3 per group). Data are represented as mean±SEM. (E–K) Pooled data from ≥2 independent experiments (n≥3 per group). Results are expressed as mean±SEM. (C–D) Two-way analysis of variance. (E–K) Two-tailed Student's t-test. ns, not significant; *p<0.05; **p<0.01; ***p<0.001; ****p<0.0001. See also online supplemental figure S1. ELISpot, Enzyme-linked immunosorbent spot; IFN, interferon; MHC, major histocompatibility complex; NeoAg, neoantigens; pMHC, peptide:MHC.

Clonal expression of weak and strong NeoAg enhances CD8+ T-cell responses against weak NeoAg

Stronger T-cell responses against weak NeoAg were consistently observed when these were clonally expressed with a strong NeoAg. This NeoAg synergy pattern was observed across multiple independent combinations of weak and strong NeoAg (figure 1E). In the same setting, T-cell responses against the strong NeoAg benefited to a lesser extent (figure 1F). Co-expression of two weak NeoAg on the other hand did not induce synergistic effects, suggesting that one potent NeoAg response was required to initiate the observed effects. In contrast, we observed a diminished W_1 response in clonal W_1-W_2 tumors, suggesting competition between the two "weak" T-cell responses (online supplemental figure S1F) in the absence of a strong NeoAg. Notably, NeoAg synergy depended on clonal NeoAg expression and was absent in subclonal expression of the same NeoAg pairs (figure 1G,H). Moreover, the lower NeoAg density in tumors with subclonal NeoAg expression (clonal fractions of 50%) was associated with overall weaker responses against all NeoAg (figure 1G–H, online supplemental figure S1G).

Clonal expression of strong NeoAg induces immunodominance in an MHC allele-dependent manner

Contrasting the synergistic effects mutually benefiting weak and strong NeoAg responses when expressed clonally, we observed an establishment of immunodominance hierarchies between concurrent T-cell responses against two strong, clonal NeoAg. Subdominance in these hierarchies weakened respective immune responses, whereas the dominant response remained unaffected. Competition between T-cell responses was thereby dependent on clonal expression and restriction to the same MHC allele (figure 1I–K). In line with previous reports,[7 54] immunodominance was established by the NeoAg with the most favorable pMHC binding characteristics (online supplemental figure S1D).

The consistent patterns of interplay observed between concurrent T-cell responses and their dependence on NeoAg clonality indicated that NeoAg expression patterns in the tumor directly impact the strength of respective T-cell responses.

Synergy between CD8+ T-cell responses enhances T-cell expansion and functionality

Next, we used the two NeoAg model systems to study NeoAg synergy in detail. To this end, we profiled $CD8^+$ T-cell responses against the strong NeoAg $S_{1\ (Adpgk)}$ and the weak NeoAg $W_{2\ (Cpne1)}$, when these were expressed either alone (strong NeoAg and weak NeoAg tumors, respectively) or in clonal, synergistic combination (NeoAg synergy tumors). Although expression of the weak NeoAg alone did not improve tumor control in outgrowth studies, NeoAg synergy tumors expressing both NeoAg were better controlled than strong NeoAg tumors (figure 2A). To resolve which NeoAg-specific response was mediating this effect, we performed adoptive $CD8^+$ T-cell transfer (ACT) experiments in $Rag2^{-/-}$ mice bearing single NeoAg-expressing tumors on opposite flanks. ACT from donors injected with NeoAg synergy tumors slowed the outgrowth of weak NeoAg tumors in $Rag2^{-/-}$ mice, whereas ACT from donors injected with weak NeoAg tumors did not (figure 2B, left panel). This suggested that the establishment of a productive T-cell response against the weak NeoAg depended on NeoAg synergy. In contrast, ACT was only minimally more efficacious in controlling strong NeoAg tumors in $Rag2^{-/-}$ mice when donors were injected with NeoAg synergy rather than strong NeoAg tumors (figure 2B, right panel). Augmented tumor control in the context of ACT from NeoAg synergy tumor-bearing donors was thus notable particularly for the immune response against the weak NeoAg (figure 2B).

Analysis of $CD8^+$ T-cell expansion kinetics in the tdLN revealed that NeoAg synergy induced a greater expansion of both NeoAg-specific T-cell responses, particularly at early time points (figure 2C), with similar kinetics observed in the spleen (online supplemental figure S2A). In line with the greater T-cell expansion in the tdLN, NeoAg synergy induced a greater infiltration of NeoAg-specific and overall $CD8^+$ T cells into the tumor (figure 2D). Functionally, in vivo cytotoxicity assays showed a significant increase in killing capacity for both T-cell responses when mice were bearing NeoAg synergy tumors (figure 2E, online supplemental figure S2B) compared with weak NeoAg and strong NeoAg tumors. Phenotypically, NeoAg-specific T cells showed higher expression of effector molecule granzyme B (GzmB) in NeoAg synergy tumors compared with respective single NeoAg-expressing tumor controls (figure 2F). Generally, the response to the weak NeoAg showed a stronger relative benefit from NeoAg synergy than the response to the strong NeoAg (online supplemental figure S2C).

As NeoAg synergy resembled $CD4^+$ T cell-mediated help,[55] we next compared the effects of NeoAg synergy to canonical $CD4^+$ T-cell help using the naturally presented, MHC-II-restricted NeoAg integrin $ß1^{N710Y}$ (Intb1).[20] IFN-γ ELISpot assays showed that $CD4^+$ T-cell help similarly induced a greater expansion of the T-cell response against the weak NeoAg (online supplemental figure S2D). Notably, $CD4^+$ T cell-mediated help depended on clonal NeoAg expression in the tumor and was absent in the case of subclonal NeoAg expression (online supplemental figure S2E), mirroring the observations made for synergistic, MHC-I-restricted NeoAg (figure 1E–H, figure 2A–F).

Synergistic effects are induced by highly stimulatory cDC1 in the tdLN mirroring NeoAg expression patterns of the tumor

Because NeoAg synergy was observed at early time points (figure 2C) and in circulation (figure 2E), we hypothesized that it could be induced during T-cell priming in the tdLN. We therefore analyzed NeoAg presentation patterns of cDC1 in the tdLN in tumors

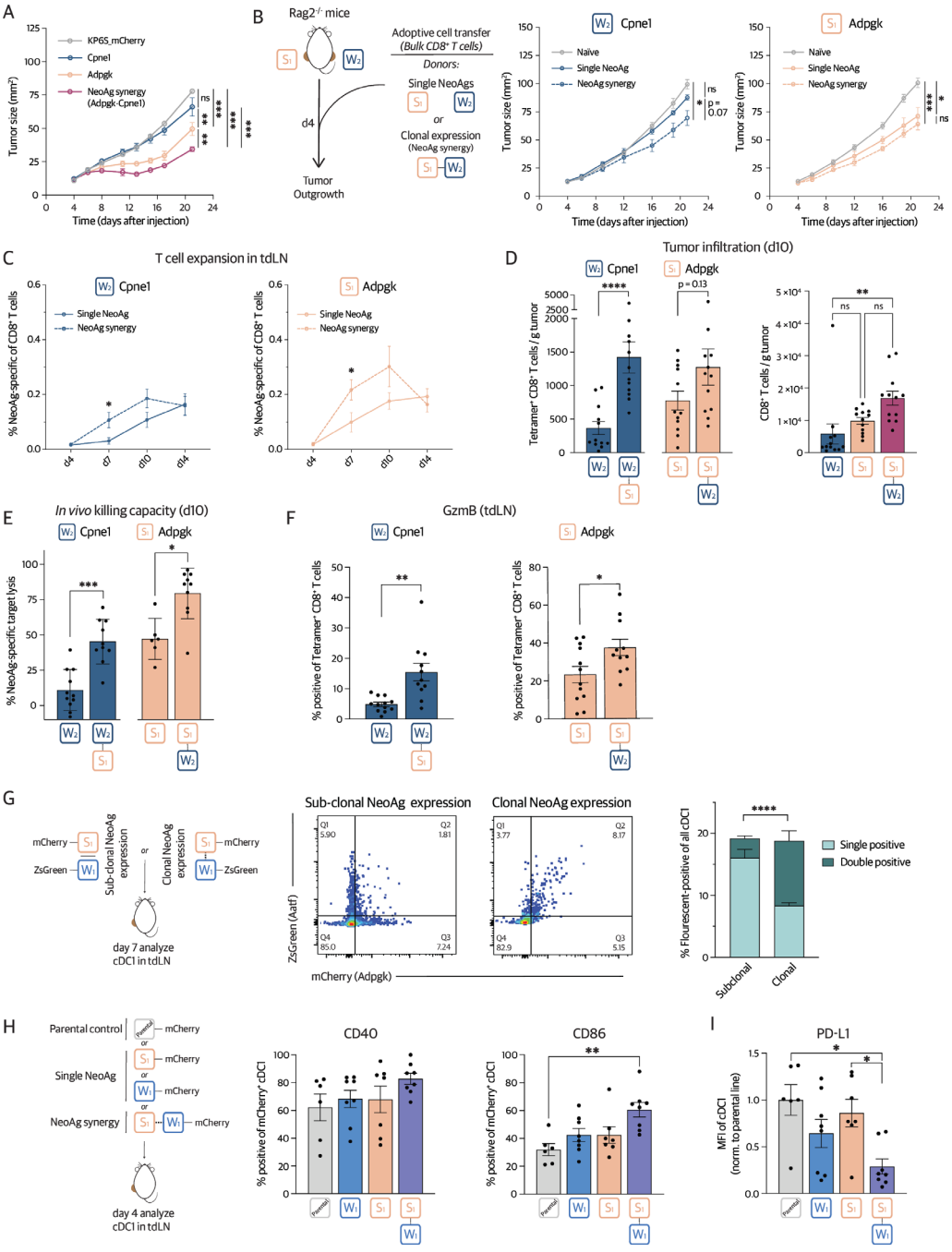

Figure 2 Synergy between CD8$^+$ T-cell responses enhances T-cell expansion and functionality. (A) Tumor outgrowth of the parental cell line, single NeoAg and NeoAg synergy tumors. (B) Tumor outgrowth in Rag2$^{-/-}$ mice following ACT on day 4 from naïve donors or from donors bearing single NeoAg or NeoAg synergy tumors. (C) Flow cytometry-based assessment of NeoAg-specific CD8$^+$ T-cell expansion in the tdLN of mice injected with single NeoAg or NeoAg synergy tumors. (D) Flow cytometry-based assessment of (left panel) NeoAg-specific and (right panel) overall CD8$^+$ T-cell tumor infiltration in mice injected with single NeoAg or NeoAg synergy tumors. (E) In vivo killing capacity of mice bearing single NeoAg or NeoAg synergy tumors on day 10 after tumor injection. (F) Flow cytometry-based analysis of GzmB expression of $S_{1\ (Adpgk)}$-specific and $W_{2\ (Cpne1)}$ -specific CD8$^+$ T cells in the tdLN in mice injected with single NeoAg or NeoAg synergy tumors. (G) Flow cytometry-based assessment of tumor debris uptake of cDC1 on day 7 after injection of tumors with clonal and subclonal NeoAg expression. (H–I) Flow cytometry-based assessment of expression of (H) co-stimulatory and (I) inhibitory markers of cDC1 engulfing debris from the parental line, single NeoAg or NeoAg synergy tumors on day 4 after tumor injection. (A–B) Representative display of ≥2 independent experiments. Data are represented as mean±SEM. (C–I) Pooled data from ≥2 independent experiments (n≥3 per group). Results are expressed as mean±SEM. (A–B) Two-way ANOVA. (C,F,G) Two-tailed Student's t-test. (D left panel), (E) Mann-Whitney U test. (D right panel), (H–I) One-way ANOVA. ns, not significant; *p<0.05; **p<0.01; ***p<0.001; ****p<0.0001. See also online supplemental figure S2 and S3. ANOVA, analysis of variance; cDC1, cross-presenting dendritic cells; GzmB, granzyme B; MFI, Median fluorescence intensity; NeoAg, neoantigens; PD-L1, programmed death-ligand 1; tdLN, tumor-draining lymph node.

with clonal and subclonal NeoAg expression (online supplemental figure S2F). To this end, we generated cell lines in which each NeoAg was fused to a separate fluorophore, enabling the use of acquired fluorescence as a surrogate for the engulfment of NeoAg-containing tumor debris, and ultimately NeoAg cross-presentation. As previously reported by our group,[8] cDC1s positive for both fluorescent proteins, a surrogate for simultaneous engulfment and processing of both NeoAg, were predominantly observed in tumors with clonal NeoAg expression and almost absent in the case of subclonal NeoAg expression (figure 2G). This suggested that cDC1 engulf tumor debris from a limited number of tumor cells before migrating to the tdLN, thus retaining the NeoAg expression pattern observed in the tumor. This further suggested that concurrent priming of different NeoAg-specific T-cell populations by the same cDC1 is limited to clonal NeoAg, potentially explaining observed synergistic effects. Phenotypic analysis of tumor-debris engulfing cDC1 revealed that simultaneous processing and presentation of synergistic NeoAg, but not of single NeoAg was associated with a highly stimulatory phenotype. When compared with cDC1 engulfing debris from the parental tumor cell line, higher surface expression of co-stimulatory molecules CD40, CD80 and CD86 and lower expression of immunoregulatory molecule PD-L1 was observed (figure 2H,I, online supplemental figure S3A). Of note, we previously demonstrated that this observation similarly applied to cDC1 co-presenting synergistic antigens derived from distinct subclones in genetically heterogenous tumors.[8] In line with the earlier expansion observed for T-cell responses in NeoAg synergy, these differences in cDC1 phenotype were observed particularly at early time points (day 4 after tumor injection, figure 2H,I) and were less pronounced at later time points (day 7 after tumor injection, online supplemental figure S3B,C). Global $CD4^+$ T-cell expansion and programmed cell death protein-1 (PD-1) expression were similar in tdLN of single NeoAg and NeoAg synergy tumors (online supplemental figure S3D), arguing against inadvertently generated MHC-II NeoAg in either cell line. To further assess whether enhanced cDC1 activation in NeoAg synergy tumors was mediated by cDC1:$CD8^+$ T-cell interactions, we performed allele-specific H2-Kb in vivo blocking experiments in W_2-S_3 (restricted to H2-Db and H2-Kb, respectively; online supplemental figure S1D) NeoAg synergy tumors (online supplemental figure S3E,F). Allele-specific blockade of H2-Kb here abrogated the NeoAg synergy effect on cDC1 activation (online supplemental figure S3E) as well as on the expansion of the weak W_2-NeoAg response (online supplemental figure S3F), indicating that these were mediated by the S_3-specific immune response.

In summary, our data demonstrate that cDC1 mirror the tumor NeoAg architecture, which limits simultaneous cDC1-mediated priming of T cells with different specificities to clonal NeoAg. Clonal expression of synergistic NeoAg is associated with a more stimulatory cDC1 phenotype, as well as enhanced T-cell expansion, tumor infiltration, effector functionality and tumor control.

Loss of synergy in tumors with heterogenous NeoAg expression leads to immunoediting and enables immune evasion

Next, we interrogated how synergy between NeoAg-specific T-cell responses impacts antitumor immunity in tumors with heterogenous NeoAg expression. To this end, we designed a tumor model with a highly synergistic NeoAg architecture encompassing the strong NeoAg $S_{1\ (Adpgk)}$ and the two weak NeoAg $W_{1\ (Aatf)}$ and $W_{2\ (Cpne1)}$. We then compared immune responses and immune-mediated tumor control between tumors with clonal (Syn_clonal tumors) and heterogenous (Syn_subclonal tumors) expression of the same NeoAg. Informed by clinical data,[9 10] Syn_subclonal tumors were designed to consist of two subclones expressing shared as well as private NeoAg with either the strong or a weak NeoAg expressed subclonally at similar levels (Syn_S_1-subclonal and Syn_W_2-subclonal, respectively, figure 3A, online supplemental figure S4A).

In line with previous studies,[56] tumor outgrowth analyses revealed that both tumors with a clonal expression of the strong NeoAg (Syn_clonal and Syn_W_2-subclonal tumors) were well controlled. Tumors with subclonal expression of the strong NeoAg (Syn_S_1-subclonal) however grew out after an initial period of control (figure 3B). Time course analysis of the tumor composition revealed that this was due to poor control of the subclone lacking expression of the strong NeoAg S_1 (figure 3C), while no immunoediting was observed in Syn_W_2-subclonal tumors (online supplemental figure S4B). Immunoediting and poor control of the subclone lacking expression of the strong NeoAg S_1 (subclone 2) in Syn_S_1-subclonal tumors is in line with previous reports[8 9 57 58] and indicated that S_1 was the main NeoAg required for tumor control in this model. However, analysis of the antitumor immune response in Syn_clonal and Syn_S_1-subclonal tumors suggested the reduction of NeoAg synergy as an additional factor enabling subclonal immune escape. In vivo cytotoxicity as well as IFN-γ ELISpot assays here showed that synergistic effects tended to be reduced in Syn_S_1-subclonal tumors (figure 3D, online supplemental figureS4C,D). Metastasis model experiments allowing to pre-establish T-cell responses to weak NeoAg showed similar control of subclone 2 in mice bearing Syn_clonal and Syn_S_1-subclonal primary tumors (injected 5 days earlier), suggesting that poor control of subclone 2 in Syn_S_1-subclonal tumors was predominantly due to a quantitative rather than qualitative impairment of the weak NeoAg-specific T-cell responses (online supplemental figure S4E). In line with the observation regarding the impact of tumor debris-engulfment on cDC1 phenotypes (figure 2H,I), we observed two differentially activated

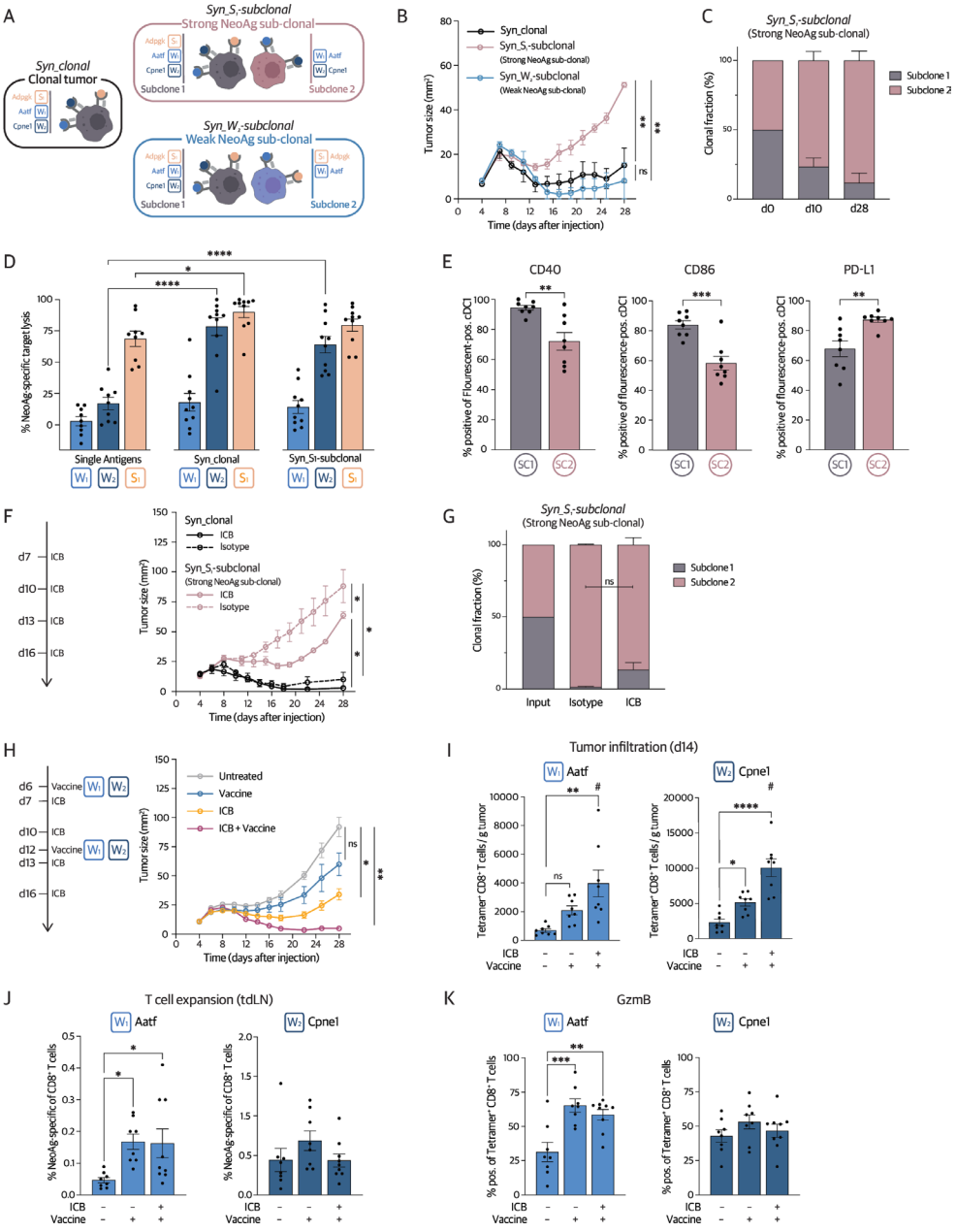

Figure 3 Loss of synergy in tumors with heterogenous NeoAg expression enables immune evasion but is overcome by therapeutic vaccination. (A) Tumor models expressing a synergistic combination of NeoAg either clonally (Syn_clonal, black box) or with the strong (Syn_S_1-subclonal, rose box) or a weak NeoAg (Syn_W_2-subclonal, blue box) expressed subclonally. (B) Tumor outgrowth of tumors in B6 mice. (C) Composition of Syn_S_1-subclonal tumors at indicated time points. (D) In vivo killing capacity of mice bearing single NeoAg, Syn_clonal or Syn_S_1-subclonal tumors on day 10 after tumor injection. (E) Flow cytometry-based assessment of co-stimulatory (CD40, CD86) and inhibitory (PD-L1) marker expression of cDC1 engulfing debris from different subclones in Syn_S_1-subclonal tumors on day 4 after tumor injection. (F) Treatment regimen and tumor outgrowth of Syn_clonal and Syn_S_1-subclonal tumors treated with dual ICB (α-cytotoxic T-lymphocyte associated protein 4 + αPD-L1) or isotype control. (G) Composition of Syn_S_1-subclonal tumors on day 28 following treatment with dual ICB. (H) Treatment regimen and tumor outgrowth of Syn_S_1-subclonal tumors in untreated mice as well as in mice treated with RNA vaccination (targeting $W_{1\ (Aatf)}$ and $W_{2\ (Cpne1)}$), dual ICB, or RNA vaccination+dual ICB. (I) Flow cytometry-based assessment of NeoAg-specific $CD8^+$ T-cell tumor infiltration of treated and untreated Syn_S_1-subclonal tumor-bearing mice. #One mouse had rejected the tumor at the time of analysis. (J) Flow cytometry-based assessment of NeoAg-specific $CD8^+$ T-cell expansion in the tdLN of treated and untreated Syn_S_1-subclonal tumor-bearing mice. (K) Flow cytometry-based assessment of effector molecule GzmB expression of NeoAg-specific $CD8^+$ T cells in the tdLN of treated and untreated Syn_S_1-subclonal tumor-bearing mice. (B,F,G) Representative display of ≥2 independent experiments. Data are represented as mean±SEM. (C–E,H–K) Pooled data from ≥2 independent experiments (n≥3 per group). Results are expressed as mean±SEM. (B,F,H) Two-way ANOVA. (E,I–K) One-way ANOVA (G) Two-tailed Student's t-test. ns, not significant; *p<0.05; **p<0.01; ***p<0.001; ****p<0.0001. See also online supplemental figure S4. ANOVA, analysis of variance; cDC1, cross-presenting dendritic cells; ICB, immune checkpoint blockade; NeoAg, neoantigens; PD-L1, programmed death-ligand 1; tdLN, tumor-draining lymph node.

cDC1 populations in the tdLN of Syn_S_1-subclonal tumors (figure 3E). Here, engulfment of debris from the subclone expressing both strong and weak NeoAg (subclone 1) was associated with significantly higher expression of co-stimulatory and lower expression of inhibitory molecules compared with cDC1 in the same tdLN engulfing debris from the subclone lacking expression of the strong NeoAg (subclone 2). This suggested that in Syn_S_1-subclonal tumors, only a fraction of cDC1 was able to mediate synergistic effects, reducing the overall immunogenicity of tumors with heterogenous NeoAg expression.

Therapeutic vaccination combined with ICB enables control of tumors with heterogenous NeoAg expression

We next interrogated the ability of different immunotherapy approaches to improve control of Syn_S_1-subclonal tumors. In line with observations made for human patients with lung cancer linking subclonal NeoAg expression to poor responses to ICB,[9 16] ICB alone failed to induce control of the tumor with heterogenous NeoAg expression (figure 3F). While ICB improved initial tumor control, Syn_S_1-subclonal continued to grow out progressively after an initial response. Tumor composition analyses showed that immunoediting occurred similarly to untreated tumors (figure 3G), demonstrating that responses against the clonal, weak NeoAg in these tumors did not sufficiently benefit from ICB. Aiming to guide the immune response towards clonal NeoAg, we then used therapeutic vaccination targeting the two weak, clonal NeoAg. To this end, we used LNP of replicon-RNA encoding for W_1 and W_2. While RNA vaccination alone induced a negligible benefit in this model, therapeutic vaccination combined with ICB showed additive effects on tumor control (figure 3H, online supplemental figure S4F). Analysis of the antitumor immune response in untreated and treated mice showed that RNA vaccination alone was sufficient to augment tumor infiltration for both targeted T-cell responses, which was further potentiated through the combination with ICB (figure 3I). Vaccination further led to a greater expansion of W_1-specific T cells with higher GzmB expression in the tdLN, suggesting superior effector functionality (figure 3J,K). In summary, therapeutic vaccination showed additive effects with ICB to enhance T-cell responses against weak NeoAg and improved tumor control, thereby overcoming the impaired immunogenicity of tumors with heterogenous NeoAg expression.

Competition between NeoAg impairs expansion and functionality of the subdominant T-cell response

Next, we analyzed how immunodominance hierarchies impact NeoAg-specific T-cell responses in tumors with competing NeoAg, focusing on the H2-Db-restriced NeoAg $S_{1\ (Adpgk)}$ and $S_{2\ (Spb2)}$. Again, we profiled T-cell responses when NeoAg were expressed alone (dom_NeoAg and subdom_NeoAg tumors for S_1 and S_2-expressing tumors, respectively) or clonally co-expressed (NeoAg competition tumors). ACT experiments using $Rag2^{-/-}$ mice bearing single NeoAg-expressing tumors on opposite flanks demonstrated that immunodominance enhanced the ability to control tumors expressing the dominant NeoAg (figure 4A, left panel), while impairing control of tumors expressing the subdominant NeoAg (figure 4A, right panel). Given the striking observation that bulk $CD8^+$ ACT from NeoAg competition tumor-bearing mice was inferior in controlling subdom_NeoAg tumors, we next assessed whether this was due to a reduced effector functionality of $S_{2\ (Spb2)}$-reactive T cells. To this end, we repeated the ACT experiments with tetramer-sorted, $S_{2\ (Spb2)}$-reactive T cells in tumor-bearing $Rag2^{-/-}$ mice. Number-matched transfer of S_2-reactive T cells from subdom_NeoAg tumors here enabled better control of S_2-expressing tumors compared with transfer from *N*eoAg competition tumors (figure 4B), suggesting that subdominance not only impairs T-cell expansion, but further negatively impacts the effector functionality.

Assessment of tumor-infiltrating T cells showed only a modest decrease in tumor infiltration for the subdominant T-cell response in NeoAg competition tumors (figure 4C), while analysis of NeoAg-specific T cells' expansion kinetics in the tdLN showed that subdominance was associated with an impaired T-cell expansion at early time points (figure 4D). Inverse changes were observed for the immunodominant NeoAg, as immunodominance was associated with enhanced early T-cell expansion (figure 4D). Expansion kinetics in the spleen mirrored these observations (online supplemental figure S5A). Phenotypically, the subdominant T-cell response was characterized by lower expression of GzmB, suggesting inferior effector functionality, whereas the immunodominant response showed no significant difference between conditions (figure 4E). In line with the phenotypic observation, in vivo cytotoxicity assays showed an increase in cytotoxic capacity for the immunodominant response, whereas the subdominant response appeared unaltered (figure 4F). A significantly impaired in vivo killing capacity of the subdominant response however was observed when assessing the impact of subdominance for the competing H2-Kb-restricted NeoAg $S_{3\ (Lama4)}$ and $S_{4\ (Alg8)}$ (online supplemental figure S5B).

Competition for MHC binding reduces subdominant NeoAg presentation by antigen-presenting cells

Establishment of immunodominance hierarchies was dependent on clonal NeoAg expression in the tumor and restriction to the same MHC allele (figure 1I–K). In combination with the observed NeoAg presentation patterns of cDC1 in the tdLN (figure 2G) and our observations that immunodominance is established in the tdLN rather than the tumor (figure 4A–F), this suggested competition for MHC binding on antigen-presenting cells (APC) as a potential mechanism underlying immunodominance. We thus quantitatively assessed the MHC-I presentation of the subdominant NeoAg on BMDCs in the presence or absence of immunodominant competition (figure 4G).

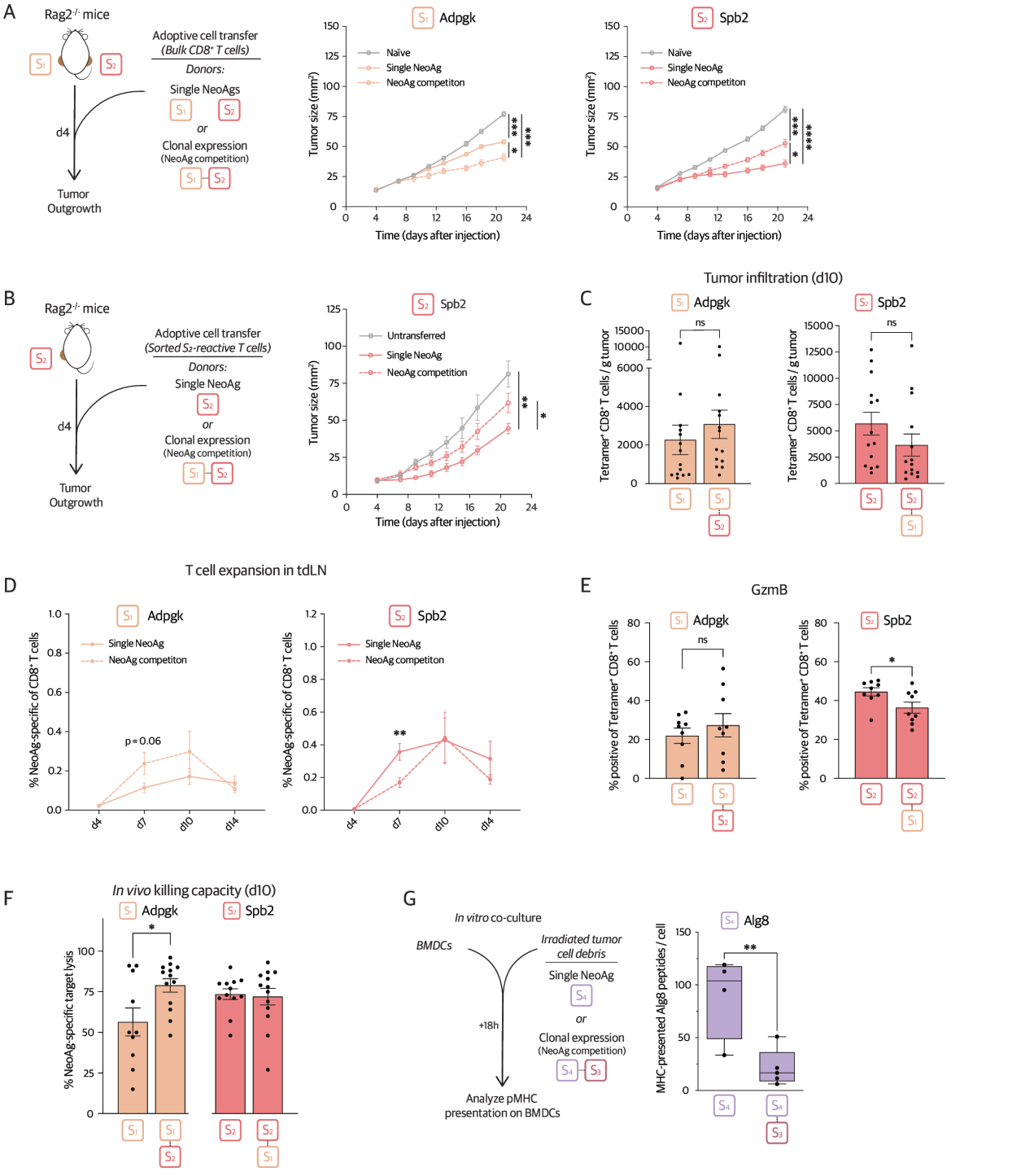

Figure 4 Competition between NeoAg impairs expansion and functionality of the subdominant T-cell response. (A) Tumor outgrowth in Rag2$^{-/-}$ mice following ACT on day 4 from naïve donors or from donors bearing single NeoAg or NeoAg competition tumors. (B) Tumor outgrowth in Rag2$^{-/-}$ mice following ACT of $S_{2\ (Spb2)}$ -specific CD8$^+$ T cells on day 4 from donors bearing single NeoAg or NeoAg competition tumors as well as untransferred control. (C) Flow cytometry-based assessment of NeoAg-specific CD8$^+$ T-cell tumor infiltration in mice injected with single NeoAg or NeoAg competition tumors. (D) Flow cytometry-based assessment of NeoAg-specific CD8$^+$ T-cell expansion in the tdLN of mice injected with single NeoAg or NeoAg competition tumors. (E) Flow cytometry-based assessment of GzmB expression of $S_{1\ (Adpgk)}$ and $S_{2\ (Spb2)}$ -specific CD8$^+$ T cells in the tdLN in mice injected with single NeoAg or NeoAg competition tumors. (F) In vivo killing capacity of mice bearing single NeoAg or NeoAg competition tumors on day 10 after tumor injection. (G) Quantitative MS-based analysis of NeoAg presentation on BMDCs co-cultured with irradiated tumor cell debris from single NeoAg or NeoAg competition tumors. (A–G) Pooled data from ≥2 independent experiments (n≥3 per group). Results are expressed as mean±SEM. (A–B) Two-way analysis of variance. (C–G) Two-tailed Student's t-test. ns, not significant; *p<0.05; **p<0.01; ***p<0.001; ****p<0.0001. See also online supplemental figure S5. ACT, adoptive cell transfer; BMDC, bone marrow-derived dendritic cell; GzmB, granzyme B; MS, Mass-spectrometry; NeoAg, neoantigens; tdLN, tumor-draining lymph node.

For technical reasons (oxidation-induced mass shift of heavy isotope-labeled peptides in methionine-containing sequences,[59] we here used the competing NeoAg pair $S_{3\ (Lama4)}$ - $S_{4\ (Alg8)}$, where S_4 had been established to be the subdominant NeoAg (figure 1I, online supplemental figure S5B). Quantitative mass spectrometry-based analysis showed that subdominance led to a drastic reduction of NeoAg presentation on BMDCs (figure 4G), supporting the competition for MHC binding at the APC level as the mechanism driving the establishment of immunodominance hierarchies. In summary, our data indicate that clonal expression of strong NeoAg restricted to the same MHC allele leads to competition for MHC binding on cDC1, quantitatively impacting NeoAg presentation and inducing the establishment of immunodominance hierarchies. Antigen hierarchies thereby favor the NeoAg best binding to its cognate MHC[7] and impair early expansion, tumor infiltration and effector functionality of subdominant T-cell responses.

Subclonal expression of immunodominant NeoAg impairs immunity and drives immune evasion

To study the significance of immunodominance hierarchies in tumors with heterogenous NeoAg expression, we next designed NeoAg architectures encompassing the competing strong NeoAg $S_{1\ (Adpgk)}$, $S_{2\ (Spb2)}$ and the weak NeoAg $W_{1\ (Aatf)}$ (Comp_tumors). When clonally expressed (Comp_clonal), an immunodominance hierarchy with S_1 as the dominant NeoAg was established between the strong NeoAg (figure 1I, figure 4). We compared the clonal tumor to subclonal tumors presenting the same set of NeoAg at similar levels (online supplemental figure S6A), with either the dominant NeoAg (Comp_S_1-subclonal) or the subdominant NeoAg (Comp_S_2-subclonal) expressed subclonally (figure 5A). Tumor outgrowth studies showed that subclonal expression of the dominant NeoAg (Comp_S_1-subclonal tumors) but not of the subdominant NeoAg (Comp_S_2-suCEclonal) led to impaired tumor control (figure 5B). Tumor composition analysis of Comp_S_1-subclonal tumors showed that impaired tumor control was due to poor control of the subclone lacking expression of the immunodominant NeoAg (figure 5C, online supplemental figure S6B). This observation was reminiscent of the observations made in tumors with heterogenous NeoAg expression bearing weak NeoAg (figure 3), suggesting two phenotypically similar yet mechanistically distinct modes of immune evasion in tumors with heterogenous NeoAg expression.

Our data suggest that immunodominance is established due to competition for MHC binding on dendritic cells (figure 1I, figure 4G). The observation that tumor NeoAg architectures are mirrored by cDC1 (figure 2H) suggested that in Comp_S_1-subclonal tumors, competition for MHC binding would be limited to cDC1 engulfing debris from subclone 1, containing both competing NeoAg. To study whether the detrimental effects of immunodominance would be mitigated in tumors with subclonal expression of the dominant NeoAg, we next compared NeoAg-specific immune responses between mice injected with Comp_clonal and Comp_S_1-subclonal tumors. In clonal tumors, in vivo cytotoxicity assays showed an enhanced killing capacity for the immunodominant NeoAg and reduced killing capacity for the subdominant NeoAg compared with mice bearing single NeoAg-expressing tumors (figure 5D). Analysis of T-cell expansion kinetics in tumor-bearing mice showed that this was associated with a suppressed expansion of the subdominant (S_2-specific) T-cell response particularly at early time points, which subsequently failed to recover despite immunoediting of subclone 1 (online supplemental figure S6C-E). Immune responses of mice bearing Comp_S_1-subclonal tumors thus mirrored those of clonal tumors, indicating that immunodominance was established to a similar extent despite subclonal expression of the dominant NeoAg (figure 5D).

Therapeutic RNA vaccination targeting the subdominant NeoAg overcomes immunodominance and induces additive effects with ICB

Whereas ICB led to the rejection of Comp_clonal tumors in most cases, Comp_S_1-subclonal tumors benefited to a lesser extent from ICB and grew out progressively after an initial phase of partial control (figure 5E). Tumor composition analyses revealed that ICB had no impact on immunoediting in these tumors, demonstrating that the subdominant T-cell response did not preferentially benefit from ICB (figure 5F, online supplemental figure S6F). Given the similarities to our observation on poor control of tumors with heterogenous NeoAg expression expressing weak NeoAg (figure 3), we reasoned that therapeutic vaccination to specifically enhance the subdominant T-cell response could be beneficial in Comp_S_1-subclonal tumors. In contrast to our observations when targeting weak NeoAg (figure 3H), targeting of the subdominant NeoAg S_2 with therapeutic replicon-RNA vaccination alone significantly improved tumor control (figure 5G). Strikingly, the combination therapy of ICB and RNA vaccination induced additive effects to further enhance immune-mediated tumor control. Analysis of T-cell expansion kinetics in the tdLN and tumor composition analyses showed that therapeutic vaccination was able to mitigate suppression of the $S_{2\ (Spb2)}$-specific T-cell response in the established immunodominance hierarchy (figure 5H,I, online supplemental figure S6G). We here observed a significantly greater expansion of the T-cell response against the vaccine-targeted NeoAg $S_{2\ (Spb2)}$. Expansion of the previously dominant NeoAg $S_{1\ (Adpgk)}$ remained similar in the context of combination therapy (figure 5H,I). Treatment further induced higher expression of the effector molecule GzmB for both T-cell responses (figure 5J). In line with the enhanced tumor control observed in mice treated with the combination of RNA vaccine and ICB, the greater expansion of NeoAg-specific T cells translated into enhanced T-cell infiltration into the tumor (figure 5K,L). Therapeutic vaccination thus effectively mitigated suppression of the subdominant

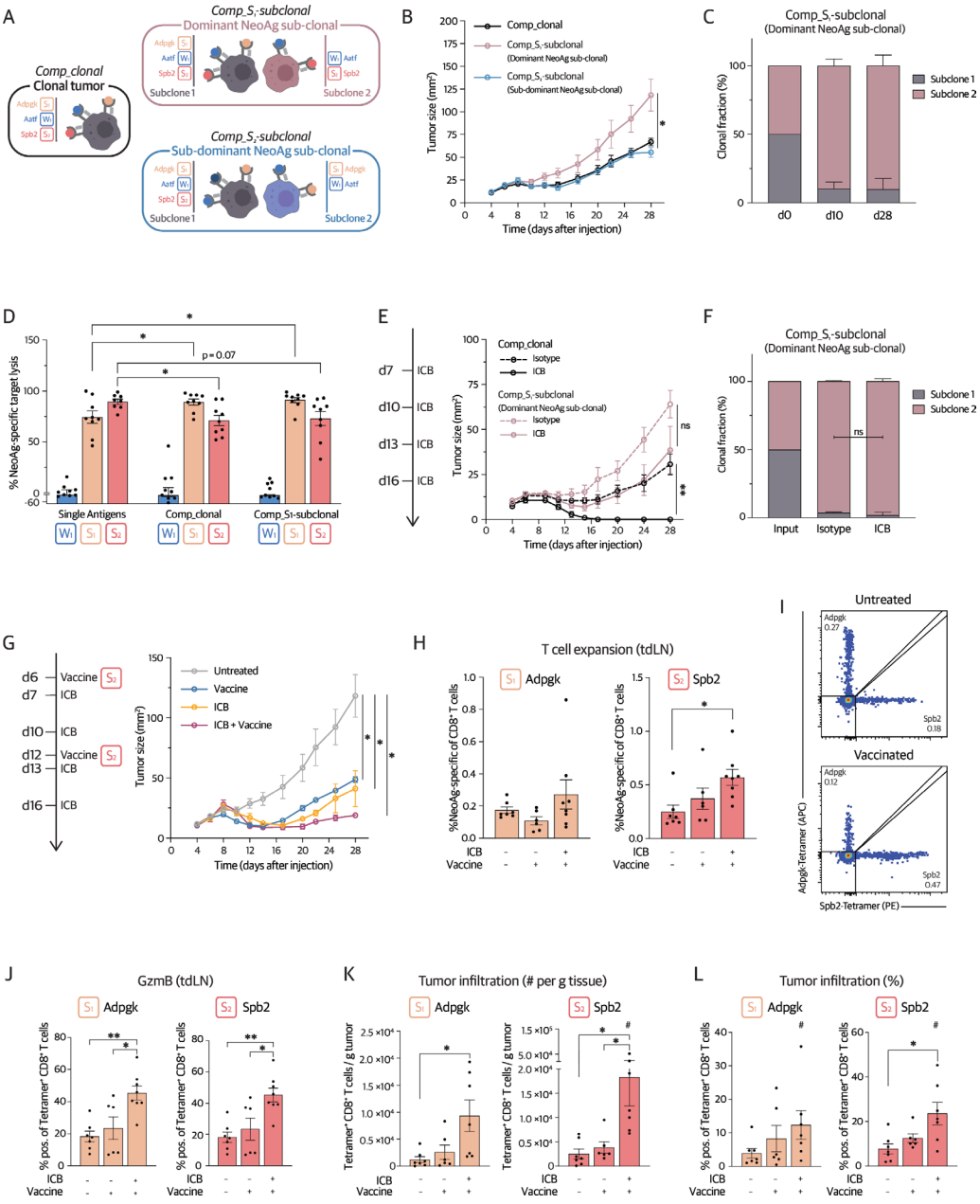

Figure 5 Subclonal expression of immunodominant NeoAg impairs immunity and drives immune evasion. (A) Tumor models expressing competing NeoAg either clonally (Comp_clonal, black box) or with the dominant (Comp_S_1-subclonal, rose box) or the subdominant NeoAg (Comp_S_2-subclonal, blue box) expressed subclonally. (B) Tumor outgrowth in B6 mice. (C) Composition of Comp_S_1-subclonal tumors at indicated time points. (D) In vivo killing capacity of mice bearing single NeoAg, Comp_clonal or Comp_S_1-subclonal tumors on day 10 after tumor injection. (E) Treatment regimen and tumor outgrowth of Comp_clonal and Comp_S_1-subclonal tumors treated with dual ICB (α-cytotoxic T-lymphocyte associated protein 4 + α-programmed death-ligand 1) or isotype control. (F) Tumor composition of Comp_S_1-subclonal tumors on day 28 following treatment with dual ICB. (G) Treatment regimen and tumor outgrowth of Comp_S_1-subclonal tumors in untreated mice as well as in mice treated with RNA vaccination (targeting $S_{2\,(Spb2)}$), dual ICB, or RNA vaccination+dual ICB. (H) Flow cytometry-based assessment of NeoAg-specific CD8$^+$ T-cell expansion in the tdLN of untreated and treated Comp_S_1-subclonal tumor-bearing mice. (I) Representative display of flow cytometry-based analysis of NeoAg-specific CD8$^+$ T-cell expansion in the tdLN in untreated and vaccinated Comp_S_1-subclonal tumor-bearing mice. (J) Flow cytometry-based assessment of GzmB expression of NeoAg-specific CD8$^+$ T cells in the tdLN of untreated and treated Comp_S_1-subclonal tumor-bearing mice. (K–L) Flow cytometry-based assessment of NeoAg-specific CD8$^+$ T-cell tumor infiltration of untreated and treated Comp_S_1-subclonal tumor-bearing mice. #One mouse had rejected the tumor at the time of analysis. (B,E–G) Representative display of ≥2 independent experiments. Data are represented as mean±SEM. (C–D,H,J–L) Pooled data from ≥2 independent experiments (n≥3 per group). Results are expressed as mean±SEM. (B,E,G) Two-way ANOVA. (F) Mann-Whitney U test. (D,H,J–L) One-way ANOVA. ns, not significant; *p<0.05; **p<0.01; ***p<0.001; ****p<0.0001. See also online supplemental figure S6. ANOVA, analysis of variance; GzmB, granzyme B; ICB, immune-checkpoint blockade; NeoAg, neoantigens; tdLN, tumor-draining lymph node.

T-cell response and enabled additive effects in combination with ICB to augment control of tumors evading the immune response due to subclonal expression of the dominant NeoAg.

NeoAg competition is dominant over NeoAg synergy in complex architectures

Our study demonstrates that the interplay between antitumor T-cell responses is dictated by NeoAg architectures and defines contextual NADi. It further indicates that different immunological mechanisms underlie the impaired immune responses towards Syn_S_1-subclonal and Comp_S_1-subclonal tumors. In both scenarios, however, therapeutic vaccination targeting clonal NeoAg synergized with ICB to significantly enhance antitumor immunity and improved tumor control. Importantly, the rules identified to govern the interplay between concurrent T-cell responses in reductionist models (figure 1E–K) remained valid in multi-NeoAg models (figure 3, figure 5). To specifically address whether immunodominance or NeoAg synergy would dominate in defining immune responses, we compared the immune response against single NeoAg to three distinct clonal tumors. Here, consistent with previous data, responses to weak NeoAg benefited from clonal expression with strong NeoAg (Syn_clonal and Syn_clonal_2 tumors, figure 6A) as NeoAg synergy enabled robust responses against multiple weak NeoAg. NeoAg synergy however was restricted to tumors lacking detectable immunodominance. NeoAg competition was thus dominant over NeoAg synergy, and no synergistic effects were observed for weak NeoAg in the presence of competing, strong NeoAg (Comp_clonal tumors, figure 6A).

Clinical data suggests immunodominance and NeoAg synergy define responsiveness to ICB in patients with cancer

To interrogate whether NADi and its impact on antitumor immunity are of similar importance in human patients with cancer, we analyzed the impact of NeoAg architectures on response to ICB in a pan-cancer cohort of >900 patients. In line with previous reports,[16] high tumor clonality was associated with response to ICB (figure 6B). Strikingly, clonality was of particular significance for strong predicted NeoAg (pNeoAg, figure 6C,D), suggesting that clonal expression of strong NeoAg with the potential to establish immunodominance hierarchies is of particular importance for the response to ICB. This observation is in line with our mouse model data showing that subclonal expression of immunodominant NeoAg can mediate resistance to ICB (figure 5E).

To survey whether weak NeoAg were able to drive responses to ICB in the context of NeoAg synergy, we next analyzed outcomes of patients with a low abundance (<median within the cohort) of strong pNeoAg. In these patients, a high abundance of weak, clonal pNeoAg was linked to response to ICB (figure 6E). Supporting the notion that clonality of weak NeoAg expression is of key importance to drive potent immune responses, ICB responders further showed a stronger correlation of overall and clonal low-affinity pNeoAg load than non-responders (figure 6F). The strong association of clonal weak NeoAg expression with response to ICB could be based on synergistic effects between clonally expressed weak NeoAg and low-abundant strong NeoAg. It further suggests that clonal weak NeoAg can effectively drive responses to ICB, supporting their role as targets for therapeutic NeoAg vaccines.

Our analysis of patient with cancer outcomes highlights the significance of NeoAg architectures for response to ICB. The refined analyses further suggest that NeoAg synergy and immunodominance are of significance in patients with cancer, as low ITH enables synergistic effects to enhance responses to weak NeoAg and circumvents suppression of T-cell responses to subclonal branches of the tumor. In summary, this suggests that the mechanisms found to define NADi and antitumor immunity in our mouse models translate to patients with cancer and could inform treatment approaches.

DISCUSSION

ITH and subclonal NeoAg expression have emerged as key determinants of potent antitumor immunity and predict response to ICB in patients with cancer.[13 16] The underlying mechanisms leading to reduced antitumor immunity in tumors with heterogenous NeoAg expression however remained poorly understood. We here uncover how NeoAg architectures affect T-cell priming by cDC1 in the tdLN to suppress NeoAg immunogenicity, thus enabling immune escape.

Antitumor T-cell immunity frequently involves concurrent recognition of multiple antigens.[3] Interplay between concurrent T-cell responses can have varying outcomes and is characterized by two overarching patterns. First, positive feedback loops enhance T-cell responses when recognition of distinct epitopes reinforces the identification of diseased cells.[55] This is best understood for $CD4^+$ T cell-mediated help, which acts through a licensing of cDC1[18 19 21 56]. Our study as well as previous work using a more reductionist approach[8] demonstrate that concurrent $CD8^+$ T-cell responses can similarly mediate synergy through a licensing of cDC1. Second, there is a preferential expansion of T-cell responses targeting epitopes with the most favorable pMHC binding characteristics, that can lead to the establishment of immunodominance hierarchies.[7 17 54] We here show that these patterns of interplay are likewise orchestrated by cDC1 mirroring tumor NeoAg architectures during T-cell priming in the tdLN.

It is conceivable that synergistic and competitive effects generally occur simultaneously during the induction of concurrent T-cell responses to clonal NeoAg. In this proposed model, NeoAg co-expression leads to the establishment of NeoAg hierarchies enhancing the immune response against the (dominant) NeoAg with the most favorable MHC binding characteristics. The outcome for non-dominant responses in these hierarchies depends

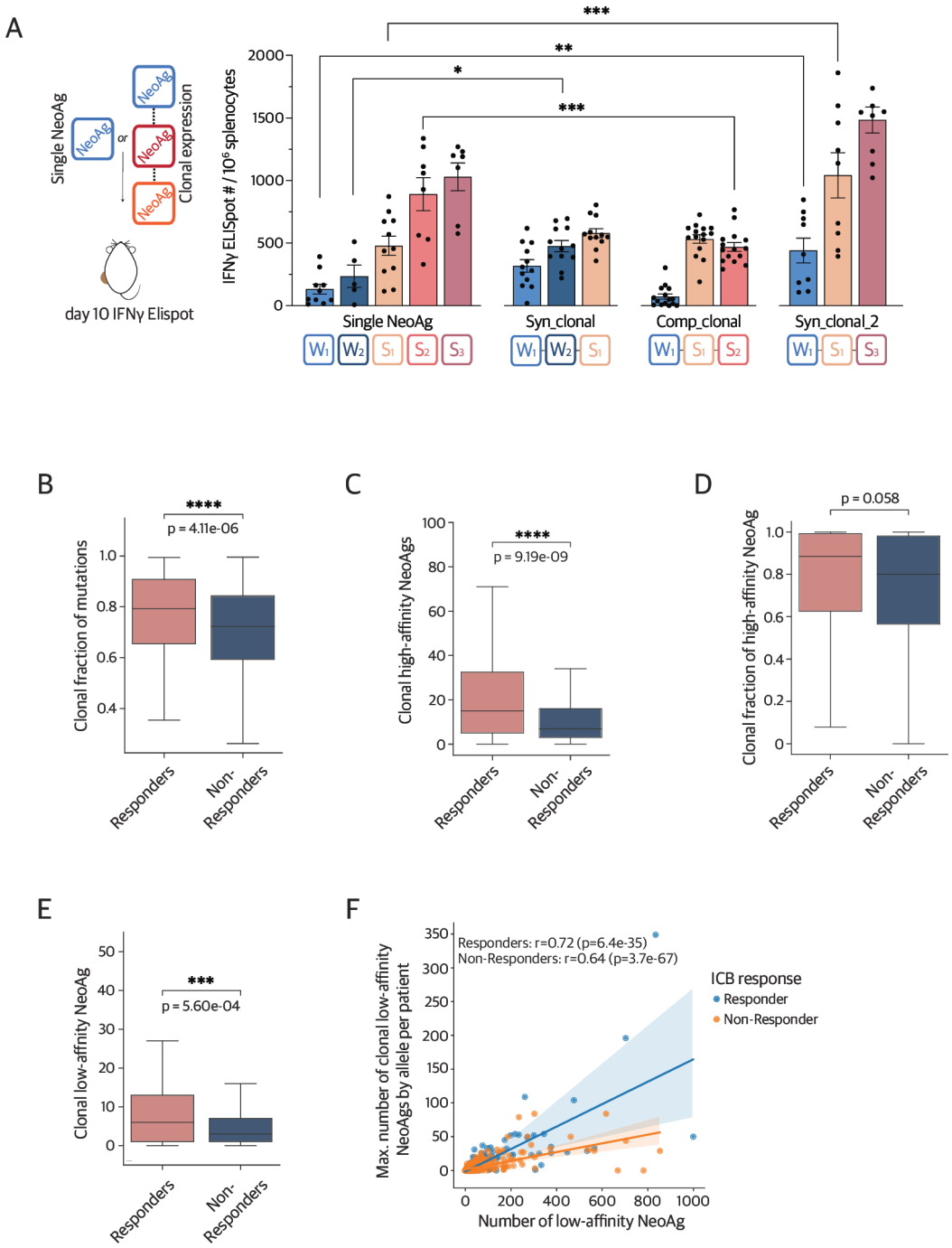

Figure 6 Clinical data suggests immunodominance and NeoAg synergy define responsiveness to ICB in patients with cancer. (A) IFN-γ ELISpot counts on day 10 after tumor injection in mice bearing single NeoAg-expressing or clonal multi-NeoAg-expressing tumors. (B) Association of tumor NeoAg clonality (fraction of mutations predicted to cluster within the same clone) and response to ICB. (C) Association of a number of clonal high-affinity NeoAg by allele and response to ICB. (D) Association of clonality of high-affinity NeoAg by allele and response to ICB. (E) Association of a number of clonal low-affinity NeoAg in patients with low (< below the median of cohort) abundance of high-affinity NeoAg and response to ICB. (F) Association of overall low-affinity pNeoAg and clonal low-affinity pNeoAg in ICB responders and non-responders. (A) Pooled data from ≥2 independent experiments (n≥3 per group). Results are expressed as mean±SEM. (A) One-way analysis of variance (Aatf, Adpgk) and two-tailed Student's t-test (Cpne1, Spb2). (B–E) Mann-Whitney U test. ns, not significant; *p<0.05; **p<0.01; ***p<0.001; ****p<0.0001. ELISpot, Enzyme-linked immunosorbent spot; ICB, immune checkpoint blockade; IFN, interferon; NeoAg, neoantigens.

on the sum of (1) synergistic effects derived from an enhanced stimulatory capacity of cDC1, which is favorable for peptides with weak MHC-I binding characteristics and (2) impaired MHC presentation and ability to expand in the tdLN, as observed for peptides competing with the dominant NeoAg for MHC-I binding. While this interplay

between T-cell responses is beneficial in clonal diseases by enhancing the most promising T-cell response, our data demonstrate that it can be detrimental for immune-mediated control of tumors with subclonal NeoAg expression.[60 61]

NeoAg synergy between responses to weak and strong NeoAg enhanced T-cell expansion, tumor infiltration, and effector functions. Importantly, both $CD8^+$ and $CD4^+$ T cell-mediated help depended on clonal NeoAg expression in the tumor, thus reducing the immunogenicity of subclonal tumors. Along with our observations on retained NeoAg presentation patterns in cDC1, this is in line with studies showing that linked NeoAg presentation by APC is required for $CD4^+$ T cell-mediated help.[21 62–64] The NeoAg synergy-induced changes in T-cell expansion kinetics, enhancing particularly early expansion, further strongly support the notion that NeoAg synergy is independent of epitope spreading.[65 66] In contrast to NeoAg synergy, which benefits multiple T-cell responses, immunodominance negatively impacts T-cell responses to subdominant, yet immunogenic NeoAg.[67] We here demonstrate that subdominance is characterized by an impairment of early T-cell expansion, tumor infiltration, and effector functionality. In line with previous reports from viral diseases,[68] the establishment of antigen hierarchies was dependent on clonal antigen expression. The observation that the establishment of antigen hierarchies is limited to NeoAg restricted to the same MHC allele and the observed reduction in MHC presentation of the subdominant NeoAg strongly suggest competition for MHC binding at the level of the APC as the underlying mechanism. Antigen-presentation by APC has previously been shown to mediate immunodominance in viral disease.[68–70] As antigen hierarchies particularly impacted early T-cell expansion, it is further conceivable that differences in naïve T-cell precursor frequencies could contribute to the establishment of immunodominance. High precursor frequency has recently been associated with immunodominance in viral disease, but its significance for mediating immunodominance in cancer remains unclear.[68 71 72]

Subclonal NeoAg have been shown to be less immunogenic than their clonal counterparts.[8 9 13 14 73] Previous studies have demonstrated that the reduced antigen density associated with subclonal NeoAg presentation impairs the potency of T-cell responses and tumor cell killing.[73 74] Beyond antigen density, our data provide evidence that unfavorable NeoAg architectures drive immune evasion of tumors with heterogenous NeoAg expression by exploiting the interplay between T-cell responses. The tumor models used in this study portray scenarios of ITH-mediated immune escape with high clinical relevance, as recent analyses have shown that most human cancers are intratumorally heterogenous and typically consist of one to three distinct subclones.[10] Subclonal NeoAg expression can be a consequence of subclonal acquisition of novel genetic alterations, immune pressure-induced loss of antigen expression or allele-specific loss of MHC expression.[75] As NeoAg synergy depends on clonal NeoAg expression in the tumor, synergistic effects derived from concurrent $CD8^+$ T-cell responses as well as from $CD4^+$ T cell-mediated help are reduced in subclonal tumors, thus impairing overall immunogenicity. This is particularly critical for tumor subclones solely expressing weak NeoAg, thus depending on help to drive potent T-cell responses. Additionally, we for the first time demonstrate that immunodominance can drive immune escape in tumors with heterogenous NeoAg expression. Immunodominant, subclonal NeoAg can suppress responses against tumor subclones lacking expression of the dominant NeoAg. By impairing the T-cell response against the subdominant NeoAg, this suppression enabled immune evasion. Surprisingly, we did not observe a potent recovery of the subdominant T-cell response following effective targeting of the dominant NeoAg, as was previously described in chronic viral disease.[76] An established immunosuppressive tumor microenvironment, including IFN-γ-induced upregulation of PD-L1 on tumor cells[77 78] following the initial immune response targeting the dominant NeoAg could explain sustained poor tumor control. However, subsequent studies will be necessary to longitudinally delineate whether shifts in immunodominance hierarchies occur after immunoediting, or whether subdominant responses continue to be impaired through other mechanisms.[79]

Clonal NeoAg have been shown to elicit robust immune responses and sensitivity to ICB. ITH on the other hand is closely associated with poor responses to ICB.[9 16] In our heterogenous tumors with immunodominance hierarchies, the subdominant T-cell response did not preferentially benefit from ICB. This is in line with clinical data and some previous mouse studies,[7 80] whereas other preclinical studies have reported a preferential benefit from ICB for subdominant T-cell responses characterized by high PD-1 expression.[60 61] ICB alone further failed to overcome the challenge of reduced NeoAg synergy in subclonal tumors. Our human data further support that both NeoAg architecture-induced synergy and immunodominance are important determinants for response to ICB in patients with cancer. In both scenarios, therapeutic vaccination targeting clonal NeoAg synergized with ICB to significantly enhance antitumor immunity and tumor control. Of note, while our NeoAg vaccines shared the premise of targeting clonal NeoAg, they were used to overcome distinct challenges associated with respective NeoAg architectures. While targeting of weak NeoAg aimed to induce responses to otherwise poorly immunogenic NeoAg, targeting of the subdominant NeoAg aimed to redirect the immune response to clonally expressed targets by mitigating the suppression in established immunodominance hierarchies. The observed synergy between NeoAg vaccines and ICB is thereby in line with previous reports on enhanced NeoAg vaccine-induced T-cell responses in the context of ICB.[81 82] NeoAg vaccines have recently shown promise in early clinical trials[83–85] and are currently tested in combination with ICB.[86 87]

Our data suggest that the composition of these typically multivalent vaccines could benefit from accounting for potential interplay between induced T-cell responses. This might allow to harness NeoAg synergy while avoiding competition between antigens and T-cell responses, with the latter achievable through spatial or temporal separation of vaccine delivery. Harnessing NeoAg architectures to maximize antitumor immunity using NeoAg vaccines will require novel bioinformatic tools to refine our vague definition of weak and strong NeoAg[88 89] to predict synergy and competition between NeoAg[90] from tumor sequencing data.

Our study establishes a comprehensive understanding of how NeoAg architectures define the immunogenicity of tumors, subclones and individual NeoAg as well as how they enable immune evasion in tumors with heterogenous NeoAg expression. Our data highlight the importance of targeting clonal NeoAg with therapeutic vaccines and demonstrate that NeoAg vaccines can synergize with ICB to enable robust control of tumors with subclonal NeoAg architectures.

Our results strongly support the conclusion that immune-mediated control of heterogenous tumors is due to NeoAg architecture-induced suppression of tumor subclone immunogenicity. Our model system however does not allow to account for cancer-immune crosstalk occurring prior to the emergence of tumor subclones. Follow-up studies using, for example, models with in vivo inducible NeoAg expression[91] could address the potential significance of such preceding cancer-immune crosstalk, ideally using autochthonous models. Additionally, it will be important to further validate the significance of the identified mechanisms in driving subclonal immune escape in human patients with cancer.

Author affiliations
[1]Koch Institute for Integrative Cancer Research, Massachusetts Institute for Technology, Cambridge, Massachusetts, USA
[2]Cancer Research UK Lung Cancer Centre of Excellence, University College London Cancer Institute, London, UK
[3]Department of Biological Engineering, Massachusetts Institute for Technology, Cambridge, Massachusetts, USA
[4]Ragon Institute at MGH, MIT and Harvard, Cambridge, Massachusetts, USA
[5]Howard Hughes Medical Institute, Chevy Chase, Maryland, USA
[6]Department of Biology, Massachusetts Institute of Technology, Cambridge, Massachusetts, USA

X Malte Roerden @RoerdenM

Acknowledgements We thank Melissa Duquette and Leon Yim for their exceptional technical support. We thank Kim Bich Nguyen for generating cell lines and critical discussions. We thank the Dong lab from Icahn School of Medicine at Mount Sinai for providing the TT3 ionizable lipid. We thank the Biopolymers & Proteomics core facility at the Koch Institute's Robert A. Swanson (1969) Biotechnology Center for excellent technical support. We thank the NIH Tetramer Core Facility (contract number 75N93020D00005) for providing Adpgk, Spb2, Cpne1 and Aatf monomers.

Contributors Conceptualization: MR, SS. Methodology: MR, ABC, YC, NH, BK, JD, LM, DJI, FW, SS. Investigation: MR, ABC, YC, NH, FW, KL. Visualization: MR, ABC. Funding acquisition: MR, SS. Project administration: SS. Supervision: SS. Writing—original draft: MR, SS. Writing—review and editing: MR, ABC, YC, NH, BK, JD, LM, FW, DJI, KL, SS. SS is the guarantor.

Funding This work was supported by the German Research Foundation (Deutsche Forschungsgemeinschaft (grant 462309583)) and by the Koch Institute Support (core) Grant P30-CA14051 (National Cancer Institute). ABC is a recipient of a Cancer Research Institute Irvington Postdoctoral Fellowship (#CRI4543). DJI is an investigator of the Howard Hughes Medical Institute.

Competing interests SS is an SAB member of Related Sciences, Arcus Biosciences, Ankyra Therapeutics, and Repertoire Immune Medicines. SS is a co-founder of Danger Bio. SS is a consultant for Takeda and Merck, and receives funding for unrelated projects from Leap Therapeutics and iTeos Therapeutics. DJI is a co-founder and consultant for Strand Therapeutics and Elicio Therapeutics. SS's and DJI's interests are reviewed and managed under MIT's policies for potential conflicts of interest. ABC is a consultant for Tempus. KL has a patent on indel burden and CPI response pending, a patent on ctDNA minimal residual disease calling methods; speaker fees from Roche tissue diagnostics and Ellipses pharma; research funding from CRUK TDL/Ono/LifeArc alliance and Genesis Therapeutics; and consulting roles with Monopteros Therapeutics, Kynos Therapeutics and Tempus Labs.

Patient consent for publication Not applicable.

Ethics approval The study was approved by MIT's Committee on Animal Care (Protocol Number 0220-006-23).

Provenance and peer review Not commissioned; externally peer reviewed.

Data availability statement Data are available upon reasonable request. Further information and requests for resources and reagents should be directed to and will be fulfilled by the corresponding author, SS (spranger@mit.edu). This study did not generate new unique reagents. This paper does not report original code. Any additional information required to reanalyze the data reported in this paper is available from the lead contact upon request.

Supplemental material This content has been supplied by the author(s). It has not been vetted by BMJ Publishing Group Limited (BMJ) and may not have been peer-reviewed. Any opinions or recommendations discussed are solely those of the author(s) and are not endorsed by BMJ. BMJ disclaims all liability and responsibility arising from any reliance placed on the content. Where the content includes any translated material, BMJ does not warrant the accuracy and reliability of the translations (including but not limited to local regulations, clinical guidelines, terminology, drug names and drug dosages), and is not responsible for any error and/or omissions arising from translation and adaptation or otherwise.

Open access This is an open access article distributed in accordance with the Creative Commons Attribution Non Commercial (CC BY-NC 4.0) license, which permits others to distribute, remix, adapt, build upon this work non-commercially, and license their derivative works on different terms, provided the original work is properly cited, appropriate credit is given, any changes made indicated, and the use is non-commercial. See http://creativecommons.org/licenses/by-nc/4.0/.

ORCID iDs
Noora Harake http://orcid.org/0009-0008-6166-1247
Stefani Spranger http://orcid.org/0000-0003-3257-4546

REFERENCES

1 Dunn GP, Old LJ, Schreiber RD. The immunobiology of cancer immunosurveillance and immunoediting. *Immunity* 2004;21:137–48.
2 Gubin MM, Artyomov MN, Mardis ER, *et al*. Tumor neoantigens: building a framework for personalized cancer immunotherapy. *J Clin Invest* 2015;125:80008:3413–21:.
3 Puig-Saus C, Sennino B, Peng S, *et al*. Neoantigen-targeted CD8$^+$ T cell responses with PD-1 blockade therapy. *Nature New Biol* 2023;615:697–704.
4 Gubin MM, Zhang X, Schuster H, *et al*. Checkpoint blockade cancer immunotherapy targets tumour-specific mutant antigens. *Nature New Biol* 2014;515:577–81.
5 Łuksza M, Riaz N, Makarov V, *et al*. A neoantigen fitness model predicts tumour response to checkpoint blockade immunotherapy. *Nature New Biol* 2017;551:517–20.
6 Balachandran VP, Łuksza M, Zhao JN, *et al*. Identification of unique neoantigen qualities in long-term survivors of pancreatic cancer. *Nature New Biol* 2017;551:512–6.
7 Burger ML, Cruz AM, Crossland GE, *et al*. Antigen dominance hierarchies shape TCF1$^+$ progenitor CD8 T cell phenotypes in tumors. *Cell* 2021;184:4996–5014.
8 Nguyen KB, Roerden M, Copeland CJ, *et al*. Decoupled neoantigen cross-presentation by dendritic cells limits anti-tumor immunity

against tumors with heterogeneous neoantigen expression. *Elife* 2023;12:e85263.
9 McGranahan N, Furness AJS, Rosenthal R, *et al*. Clonal neoantigens elicit T cell immunoreactivity and sensitivity to immune checkpoint blockade. *Science* 2016;351:1463–9.
10 Dentro SC, Leshchiner I, Haase K, *et al*. Characterizing genetic intra-tumor heterogeneity across 2,658 human cancer genomes. *Cell* 2021;184:2239–54.
11 Li Z, Seehawer M, Polyak K. Untangling the web of intratumour heterogeneity. *Nat Cell Biol* 2022;24:1192–201.
12 Vendramin R, Litchfield K, Swanton C. Cancer evolution: Darwin and beyond. *EMBO J* 2021;40:e108389.
13 Wolf Y, Bartok O, Patkar S, *et al*. UVB-Induced Tumor Heterogeneity Diminishes Immune Response in Melanoma. *Cell* 2019;179:219–35.
14 Westcott PMK, Muyas F, Hauck H, *et al*. Mismatch repair deficiency is not sufficient to elicit tumor immunogenicity. *Nat Genet* 2023;55:1686–95.
15 Rosenthal R, Cadieux EL, Salgado R, *et al*. Neoantigen-directed immune escape in lung cancer evolution. *Nature New Biol* 2019;567:479–85.
16 Litchfield K, Reading JL, Puttick C, *et al*. Meta-analysis of tumor- and T cell-intrinsic mechanisms of sensitization to checkpoint inhibition. *Cell* 2021;184:596–614.
17 Lichterfeld M, Yu XG, Le Gall S, *et al*. Immunodominance of HIV-1-specific CD8(+) T-cell responses in acute HIV-1 infection: at the crossroads of viral and host genetics. *Trends Immunol* 2005;26:166–71.
18 Ossendorp F, Mengedé E, Camps M, *et al*. Specific T helper cell requirement for optimal induction of cytotoxic T lymphocytes against major histocompatibility complex class II negative tumors. *J Exp Med* 1998;187:693–702.
19 Borst J, Ahrends T, Bąbała N, *et al*. CD4+ T cell help in cancer immunology and immunotherapy. *Nat Rev Immunol* 2018;18:635–47.
20 Alspach E, Lussier DM, Miceli AP, *et al*. MHC-II neoantigens shape tumour immunity and response to immunotherapy. *Nature New Biol* 2019;574:696–701.
21 Ferris ST, Durai V, Wu R, *et al*. cDC1 prime and are licensed by $CD4^+$ T cells to induce anti-tumour immunity. *Nature New Biol* 2020;584:624–9.
22 Yadav M, Jhunjhunwala S, Phung QT, *et al*. Predicting immunogenic tumour mutations by combining mass spectrometry and exome sequencing. *Nature New Biol* 2014;515:572–6.
23 Castle JC, Kreiter S, Diekmann J, *et al*. Exploiting the mutanome for tumor vaccination. *Cancer Res* 2012;72:1081–91.
24 Reynisson B, Alvarez B, Paul S, *et al*. NetMHCpan-4.1 and NetMHCIIpan-4.0: improved predictions of MHC antigen presentation by concurrent motif deconvolution and integration of MS MHC eluted ligand data. *Nucleic Acids Res* 2020;48:W449–54.
25 Ruhland MK, Roberts EW, Cai E, *et al*. Visualizing Synaptic Transfer of Tumor Antigens among Dendritic Cells. *Cancer Cell* 2020;37:786–99.
26 Zagorulya M, Yim L, Morgan DM, *et al*. Tissue-specific abundance of interferon-gamma drives regulatory T cells to restrain DC1-mediated priming of cytotoxic T cells against lung cancer. *Immunity* 2023;56:386–405.
27 Dolton G, Tungatt K, Lloyd A, *et al*. More tricks with tetramers: a practical guide to staining T cells with peptide-MHC multimers. *Immunology* 2015;146:11–22.
28 Ljunggren H-G, Stam NJ, Öhlén C, *et al*. Empty MHC class I molecules come out in the cold. *Nature New Biol* 1990;346:476–80.
29 Wroblewska L, Kitada T, Endo K, *et al*. Mammalian synthetic circuits with RNA binding proteins for RNA-only delivery. *Nat Biotechnol* 2015;33:839–41.
30 Li Y, Teague B, Zhang Y, *et al*. In vitro evolution of enhanced RNA replicons for immunotherapy. *Sci Rep* 2019;9:6932.
31 Li Y, Su Z, Zhao W, *et al*. Multifunctional oncolytic nanoparticles deliver self-replicating IL-12 RNA to eliminate established tumors and prime systemic immunity. *Nat Cancer* 2020;1:882–93.
32 Melo M, Porter E, Zhang Y, *et al*. Immunogenicity of RNA Replicons Encoding HIV Env Immunogens Designed for Self-Assembly into Nanoparticles. *Mol Ther* 2019;27:2080–90.
33 Fessenden TB, Stopfer LE, Chatterjee F, *et al*. Dendritic cell-mediated cross presentation of tumor-derived peptides is biased against plasma membrane proteins. *J Immunother Cancer* 2022;10:e004159.
34 Stopfer LE, Mesfin JM, Joughin BA, *et al*. Multiplexed relative and absolute quantitative immunopeptidomics reveals MHC I repertoire alterations induced by CDK4/6 inhibition. *Nat Commun* 2020;11:2760.
35 Anagnostou V, Niknafs N, Marrone K, *et al*. Multimodal genomic features predict outcome of immune checkpoint blockade in non-small-cell lung cancer. *Nat Cancer* 2020;1:99–111.
36 Rizvi NA, Hellmann MD, Snyder A, *et al*. Cancer immunology. Mutational landscape determines sensitivity to PD-1 blockade in non-small cell lung cancer. *Science* 2015;348:124–8.
37 Shim JH, Kim HS, Cha H, *et al*. HLA-corrected tumor mutation burden and homologous recombination deficiency for the prediction of response to PD-(L)1 blockade in advanced non-small-cell lung cancer patients. *Ann Oncol* 2020;31:902–11.
38 Bortolomeazzi M, Keddar MR, Montorsi L, *et al*. Immunogenomics of Colorectal Cancer Response to Checkpoint Blockade: analysis of the KEYNOTE 177 Trial and Validation Cohorts. *Gastroenterology* 2021;161:1179–93.
39 Berger MF, Hodis E, Heffernan TP, *et al*. Melanoma genome sequencing reveals frequent PREX2 mutations. *Nature New Biol* 2012;485:502–6.
40 Van Allen EM, Miao D, Schilling B, *et al*. Genomic correlates of response to CTLA-4 blockade in metastatic melanoma. *Science* 2015;350:207–11.
41 Liu D, Schilling B, Liu D, *et al*. Integrative molecular and clinical modeling of clinical outcomes to PD1 blockade in patients with metastatic melanoma. *N Med* 2019;25:1916–27.
42 Hugo W, Zaretsky JM, Sun L, *et al*. Genomic and Transcriptomic Features of Response to Anti-PD-1 Therapy in Metastatic Melanoma. *Cell* 2016;165:35–44.
43 Riaz N, Havel JJ, Makarov V, *et al*. Tumor and Microenvironment Evolution during Immunotherapy with Nivolumab. *Cell* 2017;171:934–49.
44 Snyder A, Makarov V, Merghoub T, *et al*. Genetic basis for clinical response to CTLA-4 blockade in melanoma. *N Engl J Med* 2014;371:2189–99.
45 Kim ST, Cristescu R, Bass AJ, *et al*. Comprehensive molecular characterization of clinical responses to PD-1 inhibition in metastatic gastric cancer. *Nat Med* 2018;24:1449–58.
46 Mariathasan S, Turley SJ, Nickles D, *et al*. TGFβ attenuates tumour response to PD-L1 blockade by contributing to exclusion of T cells. *Nature New Biol* 2018;554:544–8.
47 McDermott DF, Huseni MA, Atkins MB, *et al*. Clinical activity and molecular correlates of response to atezolizumab alone or in combination with bevacizumab versus sunitinib in renal cell carcinoma. *Nat Med* 2018;24:749–57.
48 Miao D, Margolis CA, Gao W, *et al*. Genomic correlates of response to immune checkpoint therapies in clear cell renal cell carcinoma. *Science* 2018;359:801–6.
49 Banchereau R, Leng N, Zill O, *et al*. Molecular determinants of response to PD-L1 blockade across tumor types. *Nat Commun* 2021;12:3969.
50 Cristescu R, Mogg R, Ayers M, *et al*. Pan-tumor genomic biomarkers for PD-1 checkpoint blockade-based immunotherapy. *Science* 2018;362:eaar3593.
51 Garcia M, Juhos S, Larsson M, *et al*. Sarek: A portable workflow for whole-genome sequencing analysis of germline and somatic variants. *F1000Res* 2020;9:63.
52 Hanssen F, Garcia MU, Folkersen L, *et al*. Scalable and efficient dna sequencing analysis on different compute infrastructures aiding variant discovery. *bioRxiv* 2023.
53 Horton BL, Morgan DM, Momin N, *et al*. Lack of $CD8^+$ T cell effector differentiation during priming mediates checkpoint blockade resistance in non-small cell lung cancer. *Sci Immunol* 2021;6:eabi8800.
54 Kaseke C, Park RJ, Singh NK, *et al*. HLA class-I-peptide stability mediates $CD8^+$ T cell immunodominance hierarchies and facilitates HLA-associated immune control of HIV. *Cell Rep* 2021;36:109378.
55 Bevan MJ. Helping the CD8(+) T-cell response. *Nat Rev Immunol* 2004;4:595–602.
56 Dunn GP, Bruce AT, Ikeda H, *et al*. Cancer immunoediting: from immunosurveillance to tumor escape. *Nat Immunol* 2002;3:991–8.
57 Zapata L, Caravagna G, Williams MJ, *et al*. Immune selection determines tumor antigenicity and influences response to checkpoint inhibitors. *Nat Genet* 2023;55:451–60.
58 DuPage M, Mazumdar C, Schmidt LM, *et al*. Expression of tumour-specific antigens underlies cancer immunoediting. *Nature New Biol* 2012;482:405–9.
59 Drazic A, Winter J. The physiological role of reversible methionine oxidation. *Biochim Biophys Acta (BBA) - Proteins Proteomics* 2014;1844:1367–82.
60 Friedman J, Moore EC, Zolkind P, *et al*. Neoadjuvant PD-1 Immune Checkpoint Blockade Reverses Functional Immunodominance among Tumor Antigen-Specific T Cells. *Clin Cancer Res* 2020;26:679–89.
61 Memarnejadian A, Meilleur CE, Shaler CR, *et al*. PD-1 Blockade Promotes Epitope Spreading in Anticancer $CD8^+$ T Cell Responses by Preventing Fratricidal Death of Subdominant Clones To Relieve Immunodomination. *J Immunol* 2017;199:3348–59.

62 Wu R, Murphy KM. DCs at the center of help: Origins and evolution of the three-cell-type hypothesis. *J Exp Med* 2022;219:e20211519.
63 Keene JA, Forman J. Helper activity is required for the in vivo generation of cytotoxic T lymphocytes. *J Exp Med* 1982;155:768–82.
64 Bennett SR, Carbone FR, Karamalis F, *et al*. Induction of a CD8+ cytotoxic T lymphocyte response by cross-priming requires cognate CD4+ T cell help. *J Exp Med* 1997;186:65–70.
65 Hu Z, Leet DE, Allesøe RL, *et al*. Personal neoantigen vaccines induce persistent memory T cell responses and epitope spreading in patients with melanoma. *Nat Med* 2021;27:515–25.
66 Brossart P. The Role of Antigen Spreading in the Efficacy of Immunotherapies. *Clin Cancer Res* 2020;26:4442–7.
67 Schreiber H, Wu TH, Nachman J, *et al*. Immunodominance and tumor escape. *Semin Cancer Biol* 2002;12:25–31.
68 Farrington LA, Smith TA, Grey F, *et al*. Competition for antigen at the level of the APC is a major determinant of immunodominance during memory inflation in murine cytomegalovirus infection. *J Immunol* 2013;190:3410–6.
69 Dinter J, Duong E, Lai NY, *et al*. Variable processing and cross-presentation of HIV by dendritic cells and macrophages shapes CTL immunodominance and immune escape. *PLoS Pathog* 2015;11:e1004725.
70 Chen W, Norbury CC, Cho Y, *et al*. Immunoproteasomes shape immunodominance hierarchies of antiviral CD8(+) T cells at the levels of T cell repertoire and presentation of viral antigens. *J Exp Med* 2001;193:1319–26.
71 Nguyen THO, Rowntree LC, Petersen J, *et al*. CD8$^+$ T cells specific for an immunodominant SARS-CoV-2 nucleocapsid epitope display high naive precursor frequency and TCR promiscuity. *Immunity* 2021;54:1066–82.
72 Kastenmuller W, Gasteiger G, Gronau JH, *et al*. Cross-competition of CD8+ T cells shapes the immunodominance hierarchy during boost vaccination. *J Exp Med* 2007;204:2187–98.
73 Westcott PMK, Sacks NJ, Schenkel JM, *et al*. Low neoantigen expression and poor T-cell priming underlie early immune escape in colorectal cancer. *Nat Cancer* 2021;2:1071–85.
74 Gejman RS, Chang AY, Jones HF, *et al*. Rejection of immunogenic tumor clones is limited by clonal fraction. *Elife* 2018;7:e41090.
75 McGranahan N, Rosenthal R, Hiley CT, *et al*. Allele-Specific HLA Loss and Immune Escape in Lung Cancer Evolution. *Cell* 2017;171:1259–71.
76 Turnbull EL, Wong M, Wang S, *et al*. Kinetics of Expansion of Epitope-Specific T Cell Responses during Primary HIV-1 Infection. *J Immunol* 2009;182:7131–45.
77 Yi M, Niu M, Xu L, *et al*. Regulation of PD-L1 expression in the tumor microenvironment. *J Hematol Oncol* 2021;14:10.
78 Garcia-Diaz A, Shin DS, Moreno BH, *et al*. Interferon Receptor Signaling Pathways Regulating PD-L1 and PD-L2 Expression. *Cell Rep* 2017;19:1189–201.
79 Dijkstra KK, Wu Y, Swanton C. The Effects of Clonal Heterogeneity on Cancer Immunosurveillance. *Annu Rev Cancer Biol* 2023;7:131–47.
80 Chen L, Azuma T, Yu W, *et al*. B7-H1 maintains the polyclonal T cell response by protecting dendritic cells from cytotoxic T lymphocyte destruction. *Proc Natl Acad Sci U S A* 2018;115:3126–31.
81 Liu L, Chen J, Zhang H, *et al*. Concurrent delivery of immune checkpoint blockade modulates T cell dynamics to enhance neoantigen vaccine-generated antitumor immunity. *Nat Cancer* 2022;3:437–52.
82 Oladejo M, Paulishak W, Wood L. Synergistic potential of immune checkpoint inhibitors and therapeutic cancer vaccines. *Semin Cancer Biol* 2023;88:81–95.
83 Rojas LA, Sethna Z, Soares KC, *et al*. Personalized RNA neoantigen vaccines stimulate T cells in pancreatic cancer. *Nature New Biol* 2023;618:144–50.
84 Ott PA, Hu Z, Keskin DB, *et al*. An immunogenic personal neoantigen vaccine for patients with melanoma. *Nature New Biol* 2017;547:217–21.
85 Keskin DB, Anandappa AJ, Sun J, *et al*. Neoantigen vaccine generates intratumoral T cell responses in phase Ib glioblastoma trial. *Nature New Biol* 2019;565:234–9.
86 Khattak A, Weber JS, Meniawy T, *et al*. Distant metastasis-free survival results from the randomized, phase 2 mRNA-4157-P201/KEYNOTE-942 trial. *J C O* 2023;41:LBA9503.
87 Burris III HA, Patel MR, Cho DC, *et al*. A phase 1, open-label, multicenter study to assess the safety, tolerability, and immunogenicity of mRNA-4157 alone in subjects with resected solid tumors and in combination with pembrolizumab in subjects with unresectable solid tumors (Keynote-603). *JGO* 2019;5:93.
88 Müller M, Huber F, Arnaud M, *et al*. Machine learning methods and harmonized datasets improve immunogenic neoantigen prediction. *Immunity* 2023;56:2650–63.
89 Łuksza M, Sethna ZM, Rojas LA, *et al*. Neoantigen quality predicts immunoediting in survivors of pancreatic cancer. *Nature New Biol* 2022;606:389–95.
90 Boulanger DSM, Eccleston RC, Phillips A, *et al*. A Mechanistic Model for Predicting Cell Surface Presentation of Competing Peptides by MHC Class I Molecules. *Front Immunol* 2018;9:1538.
91 Damo M, Fitzgerald B, Lu Y, *et al*. Inducible de novo expression of neoantigens in tumor cells and mice. *Nat Biotechnol* 2021;39:64–73.